RESEARCH   **Open Access**

Multipath exploited Bayesian and Cramér-Rao bounds for single-sensor target localization

Pawan Setlur* and Natasha Devroye

Abstract

In urban scenarios, radar returns consist of a direct path return along with multipath returns from signal reflections off surfaces such as building walls or floors. When multipath is resolvable, and given the knowledge of the geometry of the reflecting surfaces, it has recently been demonstrated that multipath returns create additional "virtual" radar sensors, thereby permitting target localization with a single radar sensor. The goal of this article is to determine theoretical variance lower bounds on how well a single-sensor system is able to localize a target in the presence of exploitable multipath and discuss several practical issues that arise in this context, including the multipath association problem, clutter, and the impact of wall roughness. Exploiting multipath, rather than viewing it strictly as a hindrance, is an emerging topic in the radar community whose potential is not yet fully understood. Towards this goal, we first derive the Cramér-Rao and the Bayesian Cramér-Rao bounds on target localization using a single-sensor which exploits resolvable multipath. For a wide class of radar-target geometries, functions termed multipath preservers are derived which indicate when multipath is physically observable in the radar returns; these functions assist in evaluating the potential of multipath exploitation in urban sensing. Given a reflecting geometry, the obtained lower bounds allow the radar operator to anticipate blind spots, place confidence levels on the localization results, and permit sensor positioning to optimally aid in exploiting multipath for target localization. It is shown that variance bounds on the location parameters improve with richer resolvable multipath generating mechanisms.

Keywords: Target localization, Radar, Multipath exploitation, Bayesian Cramér-Rao, Urban sensing, Experimental design, Statistical identifiability

1 Introduction

When radar signals are reflected from building walls in urban scenarios, multipath radar returns result, causing false positives. The objective of multipath exploitation is to identify these multipath returns, which exist because of the target and its surrounding reflecting geometry, and exploit them to improve the radar system performance. Recently, it has been noted that when multipath returns are resolvable and the reflecting surface geometry is known *a priori* (e.g., via prior surveillance), multipath radar returns create virtual radar sensors, permitting non-coherent target localization with a *single-sensor* [1]. This single-sensor localization approach may offer a viable sensing solution to modern urban sensing challenges. In other non-radar applications, such as wireless sensor

localization, the multipath also results in virtual beacons (receivers) similarly permitting localization with a single sensor.

1.1 Goal

Our goal is to better understand the fundamental limits of idealized multipath exploitation in the context of single sensor systems and to analytically discuss the system performance with practical considerations including for example, the roughness of walls and the presence of clutter. Single-sensor systems are covert, may be smaller, simpler to deploy, and more cost-effective than multi-sensor systems; however, this simplicity may come at the cost of increased signal processing complexity and/or decreased performance when compared to multi-sensor systems. As little work has emerged on single-sensor multipath exploitation, we focus on the theoretical gains possible here, which could be used as a benchmark for future multipath exploiting localization schemes.

*Correspondence: setlurp@uic.edu
Department of Electrical and Computer Engineering, University of Illinois at Chicago, Chicago, IL 60607, USA

For analytical tractability, the direct path time delay and the multipath time delays are assumed to be normally distributed perturbed versions of their true counterparts. The main crux of this article is in evaluating the potential of single-sensor-based localization from a theoretical perspective using the Cramér-Rao bounds (CRBs) and the Bayesian Cramér-Rao bounds (BCRBs). Further, the objective is also to determine spatial regions within a geometry where such systems are most beneficial in localizing targets via multipath exploitation. The former provides a lower bound on the variance of the non-coherent localization error, whereas the latter determines optimal target or sensor positions where single-sensor radar systems offer the most benefit. Neither of these have yet been addressed for a single-sensor system, and considering practical constraints in the literature.

Towards our goal, we study one particular geometry as an example: a single target enclosed in a rectangular urban canyon. The multipath generating mechanisms, i.e., the walls, are assumed to be smooth at the radar operating frequencies, resulting in specular reflections. The wall roughness and its impact on localization is handled subsequently.

1.2 Contributions
Our contributions are summarized as follows.

In the multipath exploitation literature [1-7], it is assumed that multipath returns exist; no such conditions are enforced here. Rather, we *introduce the concept of "multipath preservers"* indicating when multipath is present, which are incorporated into the subsequent theoretical analysis.

Next, we *derive the CRBs and the BCRBs for the target downrange and the crossrange using a single sensor which exploits resolvable multipath.* Using the relevant metrics from the theory of optimal experimental design [8,9], and employing the multipath preservers, the CRBs and BCRBs allow the radar operator to anticipate blind spots, permit sensor or target positioning, improve interpretability of the radar returns, and place confidence levels on single-sensor localization employing multipath exploitation. This may all be accomplished beforehand, for example during the radar resource scheduling or before deployment, since the geometry is assumed to be known *a priori*. Experimental design principles can be applied to the problem at hand since the Fisher information matrices (FIMs) are the functions of the location parameters, namely the downrange and the crossrange. It is shown that richer resolvable multipath generating mechanisms always improve target localization, in the CRB and BCRB sense.

In addition, we discuss several topics which may impact the utility of single-sensor localization: the multipath association problem (i.e., to determine which multipath return corresponds to which wall), the impact of wall roughness, and finally clutter. We provide initial directions for handling these possible impediments, and simulations which indicate their potential impact.

We note that our focus is on using the CRB and BCRB to understand and exploit the multipath, rather than on improving the estimation of the multipath or the direct path time delays, or deriving performance bounds on the time delay estimation [10]. Instead, the focus is on evaluating single-sensor localization performance bounds via multipath exploitation given a model of the estimates of the direct and multipath time delays.

1.3 Past work
Multipath exploitation in radar has been reported in the recent literature [2-7], all of which assume specular multipath. Statistical radar detection was treated in [2], target tracking in [3], airborne radar applications in [4], range-Doppler application in [5], experimental indoor multipath detection in [6], and localization, but not with a single sensor in [7]. The CRBs on the location parameters using multiple sensors were subsequently derived in [7]. Multipath in multiple sensor systems was studied in [11], where synthetic aperture multipath ghosts were observed but not exploited. Synthetic aperture through-the-wall multipath ghosts were associated and mapped back to the target locations using a technique derived in [12]. It was shown that the association and mapping increase the SNR at the target location, while simultaneously reducing the false positives in the synthetic aperture radar (SAR) image. It was shown that exploiting the multipath SAR ghosts, target classification is improved in [13].

1.4 Organization
The remainder of this article is organized as follows: the model for the single-sensor technique is described in Section 2; in Section 3, the CRBs and BCRBs are derived. Using experimental design criteria, the applications of sensor and target positioning are addressed in Section 4. Other topics such as associating the multipath to the walls, impact of the wall roughness on the multipath returns, and clutter are discussed in Section 5. Simulations are presented in Section 6, and conclusions drawn in Section 7.

2 Model
For ease of exposition we start with a single reflecting surface such as the side wall of a building as shown in Figure 1a, considered in two dimensions, with origin "O" shown. The target denoted as (T), radar (R), the virtual radar created due to the multipath w.r.t wall-1 and denoted as (VR_1) are also shown in the figure. The wall roughness is considered to be much smaller than the radar operating wavelength, and hence specular reflections are
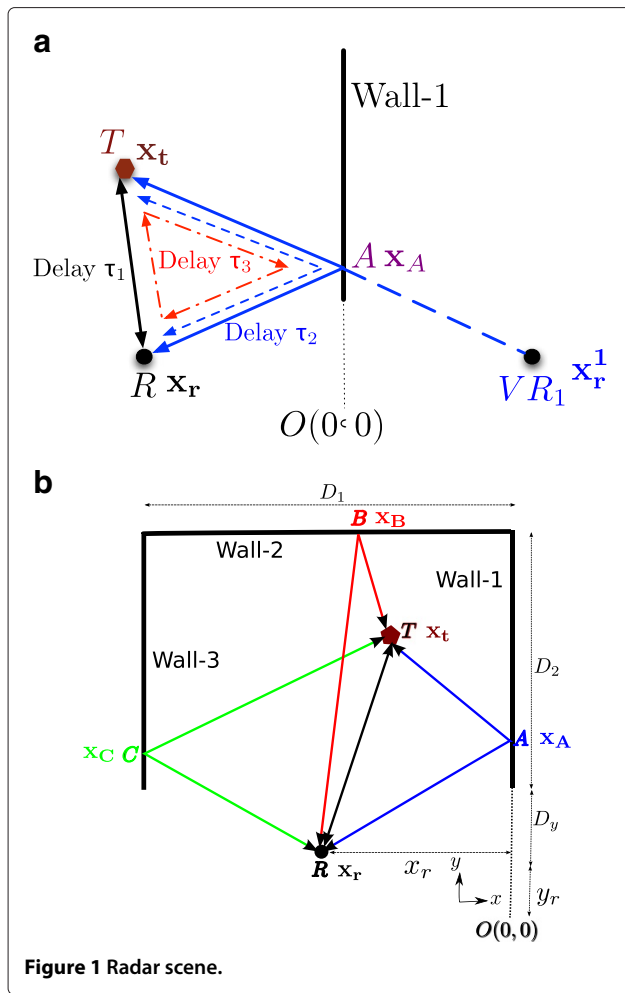
Figure 1 Radar scene.

assumed for now. The radar and target are located at $\mathbf{x_r} = [-x_r, y_r]^T$ and $\mathbf{x_t} = [-x_t, y_t]^T$. There are three paths, shown in Figure 1a, which result in time delays as follows:

$$\tau_1 = 2||\mathbf{x_t} - \mathbf{x_r}||/c, \quad \tau_2 = 2||\mathbf{x_r^1} - \mathbf{x_t}||/c,$$
$$\tau_3 = \tau_1/2 + \tau_2/2 \tag{1}$$
$$\mathbf{x_r^1} := [x_r, y_r]^T$$

where c denotes the speed of light in freespace and is assumed constant throughout. The time delays, τ_2 and τ_3 with $\tau_1 \leq \tau_3 \leq \tau_2$, are referred to as the II-order and I-order multipath, respectively. The first-order (I-order) multipath incorporates one reflection at wall-1, while the second-order (II-order) multipath incorporates two reflections at wall-1. Rewriting (1), we may express the relationship between the location and time-delay variables as

$$(x_t - x_r)^2 + (y_t - y_r)^2 = c^2\tau_1^2/4 \tag{2a}$$
$$(x_t + x_r)^2 + (y_t - y_r)^2 = c^2\tau_2^2/4 \tag{2b}$$
$$\frac{x_t^2}{c^2\tau_3^2/4} + \frac{(y_t - y_r)^2}{(c^2\tau_3^2 - 4x_r^2)/4} = 1. \tag{2c}$$

It is readily seen that (2a) and (2b) are the equations of circles, whereas (2c) is the equation of an ellipse which has its foci at the radar, $\mathbf{x_r}$ and the *virtual radar* at $\mathbf{x_r^1}$, consistent with a bistatic radar configuration. *The circles and ellipses in (2) are the loci or the iso-range contours traced by target and its multipath w.r.t wall-1* ([14], p.42). It may then be shown that the common intersection point of (2a)–(2c) is the target location $\mathbf{x_t}$. When the measured time delays $\tau_i, i = 1, 2, 3$ are substituted in (2), the target may be non-coherently localized, provided the multipath and direct path are detectable and resolvable in the range profile [1]. The multipath therefore creates *virtual* monostatic and *virtual* bistatic receivers aiding localization with a single *real* monostatic sensor. It is assumed throughout that the multipath radar returns are detectable and resolvable in this article. When this assumption is invalid, multipath exploitation becomes challenging, if possible at all. Given that multipath exploitation is still a relatively emerging topic in radar, as a first step, we are interested in determining performance bounds under idealized conditions; investigating performance under conditions when some or all the assumptions start to break down is an interesting topic for future work.

Now consider Figure 1b, which shows an urban canyon type geometry with the target inside the urban canyon, of dimension D_1 and D_2, respectively. Denote the multipath time delays generated from wall-2 as τ_4 and τ_5 ($\tau_1 \leq \tau_5 \leq \tau_4$), and wall-3 as τ_6 and τ_7 ($\tau_1 \leq \tau_7 \leq \tau_6$). The time delays τ_4 and τ_6 are similar to delay τ_2 but generated from double reflections from wall-2 and wall-3 respectively. Likewise, τ_5 and τ_7 are similar to the delay τ_3 and consist of a one-way propagation via the direct line of sight path, and a bounce on the return (or vice versa). Due to these similarities $\tau_p, p = 2, \ldots, 7$ are not explicitly shown in Figure 1b. These time delays may be expressed as follows:

$$\tau_4 = 2||\mathbf{x_r^2} - \mathbf{x_t}||/c, \ \tau_5 = \tau_1/2 + \tau_4/2,$$
$$\tau_6 = 2||\mathbf{x_r^3} - \mathbf{x_t}||/c, \ \tau_7 = \tau_1/2 + \tau_6/2 \tag{3}$$
$$\mathbf{x_r^1} := [x_r, y_r]^T, \ \mathbf{x_r^2} := [-x_r, 2D_2 + 2D_y + y_r]^T,$$
$$\mathbf{x_r^3} := [-(2D_1 - x_r), y_r]^T$$

for *virtual radars* at positions $\mathbf{x_r^j}, j = 1, 2, 3$, and the parameter D_y the *standoff distance* as shown.

2.1 Multipath preservers

Using geometric arguments we derive simple functions that indicate when multipath is present in the radar returns. In general, these functions predict spatial zones where rich multipath may be present, and which could be 'mined' for potential multipath exploitation. For sensor positioning, these functions may be used in a straightforward manner to place spatial constraints on the number of

feasible sensor positions, with the objective of maximizing the multipath exploited system performance. Further, these functions could also be used *a posteriori* in placing some confidence on the target location estimates. The formulation in (1) and (3) assumes that multipath returns are always present for each corresponding wall and was an implicit assumption in [1-7,11-13]. This is in general not true. To understand the reason, consider point A in Figure 1a, having coordinates $\mathbf{x_A} = [0, y_A]^T$, $y_A(\mathbf{x_r}, \mathbf{x_t}) := \frac{y_t x_r + x_t y_r}{x_t + x_r}$, and explicitly a function of the radar and target coordinates. Clearly, for multipath to exist for this wall, we must have that $D_y + y_r \leqslant y_A \leqslant D_2 + D_y + y_r$. We can now formulate a multipath preserving function, denoted as $f_1(y_A)$,

$$f_1(y_A) = \mathbb{1}\left[D_y + y_r \leqslant y_A \leqslant D_2 + D_y + y_r\right], \qquad (4)$$

where $\mathbb{1}[\cdot]$ is the indicator function. In essence, (4) implies that if point A is not on its respective wall, then no multipath is observed, which implies $\tau_3 = \tau_2 = 0$. In the same spirit, we may derive the multipath preserving functions for the other two walls in Figure 1b as

$$f_2(x_B) = \mathbb{1}[0 \leqslant x_B \leqslant D_1], \qquad (5)$$

$$f_3(y_C) = \mathbb{1}\left[D_y + y_r \leqslant y_C \leqslant D_2 + D_y + y_r\right], \qquad (6)$$

with coordinates

$$x_B(\mathbf{x_r}, \mathbf{x_t}) := \frac{x_r(D_2 + D_y + y_r - y_t) + x_t(D_2 + D_y)}{2D_2 + 2D_y + y_r - y_t}$$

$$y_C(\mathbf{x_r}, \mathbf{x_t}) := \frac{y_t x_r - y_t D_1 + y_r x_t - y_r D_1}{x_r + x_t - 2D_1},$$

where $\mathbf{x_B} = [-x_B, D_2 + D_y + y_r]^T$ and $\mathbf{x_C} = [-D_1, y_C]^T$ are the coordinates of points B and C in Figure 1b, respectively. The conditions in (4), (5), (6) are derived from simple geometrical constraints; hence, the coordinates of the points, A, B, C are the functions of both $\mathbf{x_t}$ and $\mathbf{x_r}$. When the need arises, their dependence on $\mathbf{x_r}$ and $\mathbf{x_t}$ will explicitly be noted.

Incorporating multiple (more than 2) reflections at multiple walls and their corresponding multipath preservers into our model is straightforward, but is not considered here as the radar returns associated with multiple reflections have low signal power due to two factors (ignoring the radar cross section of the target itself): the path loss and the reflection coefficients. The path loss is inversely proportional to a function of the distance traveled by the individual multipath. In general, for each signal reflection a fraction of the incident power is lost, and is related to the reflection coefficient for that particular wall. The reflection coefficients in turn depend on the material property of the walls as well as the incidence and refraction angles. If indeed multipath from such multiple reflections are detectable and resolvable, it may be shown from the results in the next section that localization will only improve in the CRB sense. Although not treated explicitly

here, note that inclusion of a front wall in say Figure 1b yields a through-wall radar scenario [12,15] in which case the analysis here provides a valid approximation, for example when $D_y \gg D_1, D_2$.

3 CRBs and BCRBs

We now proceed to derive expressions for lower bounds on the target localization error co-variance in classical and Bayesian settings. To do so, we express the FIM in terms of the assumed to be known (up to additive Gaussian noise) multipath delays, and incorporate the multipath preserver functions from the previous section. The target localization error covariance matrix is then lower bounded by the CRB, i.e., the inverse of the FIM. In the Bayesian setting where we assume prior statistics on the target location, the target localization error covariance is bounded by the BCRB—the inverse of the analogous Bayesian information matrix (BIM).

If $s(t)$ is the signal transmitted by the radar, then in general, the received radar return denoted by $s_r(t)$ is expressed as

$$s_r(t) = \sum_{p=1}^{7} \rho_p s(t - \tau_p) + v_n(t) + v_c(t)$$

where ρ_p captures the strength of the various direct and multipaths, $v_c(t)$ is the clutter in $s_r(t)$, and $v_n(t)$ is the noise. Although not explicitly stated, we have assumed an omni-directional radar, and in practice the ρ_p will also depend on the antenna pattern. In general, it is noted that the direct and multipath each have different SNRs as well as different signal-to-clutter ratios (SCRs) as captured by the different $\rho_p, p = 1, 2, \ldots, 7$. In essence, their individual SNRs and SCRs will affect their detectability in the range profile, and is not the focus here. In other words, we will assume that the τ_p are all detectable in the range profile. Modeling urban clutter is difficult, and moreover not straightforward to model stochastically. We will therefore ignore clutter and treat only the noise in the FIM and BIM analysis. Clutter however is discussed in Section 5, and incorporated as spurious time delays in the simulations, i.e. Section 6.

In practice, the time delays, τ_p, $p = 1, \ldots, 7$ are obtained from correlating the transmitted signal with the received radar returns, see for example [1]. It is therefore reasonable to assume that the measured time delays, denoted as ζ_p, are perturbed versions of their true counterparts. The perturbations denoted as v_p are assumed to be zero mean, normally distributed, and mutually uncorrelated random variables of variance σ_p^2. Therefore, the p-th time delay measurement, ζ_p, is given by

$$\zeta_p = f(p) \times \tau_p + v_p, \quad p = 1, 2, \cdots 7, \qquad (7)$$

where $f(1) = 1, f(2) = f(3) = f_1(y_A), f(4) = f(5) = f_2(x_B)$, and $f(6) = f(7) = f_3(y_C)$. The assumption of normality imposed on the ν_p ensure analytical tractability of the CRBs. If the τ_p are well separated in the τ domain, which is the case for large bandwidth, then the ν_p may be modeled as uncorrelated; this is our assumption.

3.1 CRBs

The CRB for target localization is given by the inverse of the FIM for target location $\mathbf{x_t}$. We break the complete FIM down into its various components, i.e., first, we examine the FIM considering only the multipath and direct path w.r.t to each wall independently. Let $\mathbf{F}_k(\mathbf{x_t})$ denote the FIM considering only wall $k = 1, 2, 3$ assuming $\mathbf{x_t^1} := [x_t, y_t]^T$, i.e., suppressing the negative sign of x_t in $\mathbf{x_t}$. Using (7) and for the time being assuming that the corresponding multipath preservers are unity,

$$\mathbf{F}_k(\mathbf{x_t}) = \left[\frac{1}{\sigma_1^2} \frac{\partial \tau_1}{\partial \mathbf{x_t^1}} \left(\frac{\partial \tau_1}{\partial \mathbf{x_t^1}} \right)^T + \left(\mathbf{G}_k(\sigma_k, \sigma_{2k+1}) \odot \frac{\partial \boldsymbol{\tau}_k}{\partial \mathbf{x_t^1}} \right) \right.$$
$$\left. \times \left(\mathbf{G}_k(\sigma_k, \sigma_{2k+1}) \odot \frac{\partial \boldsymbol{\tau}_k}{\partial \mathbf{x_t^1}} \right)^T \right] \tag{8}$$

where '$\odot$' denotes the Hadamard product or elementwise multiplication, $\boldsymbol{\tau}_k := [\tau_{2k}, \tau_{2k+1}]$, and

$$\mathbf{G}_k(\sigma_k, \sigma_{2k+1}) = \begin{bmatrix} 1/\sigma_{2k} & 1/\sigma_{2k+1} \\ 1/\sigma_{2k} & 1/\sigma_{2k+1} \end{bmatrix}, \quad k = 1, 2, 3$$

$$\frac{\partial \boldsymbol{\tau}_k}{\partial \mathbf{x_t^1}} := \left[\left(\frac{\partial \boldsymbol{\tau}_k}{\partial x_t} \right)^T, \left(\frac{\partial \boldsymbol{\tau}_k}{\partial y_t} \right)^T \right]^T \in \Re^{2 \times 2},$$

$$\frac{\partial \tau_1}{\partial \mathbf{x_t^1}} := \left[\frac{\partial \tau_1}{\partial x_t}, \frac{\partial \tau_1}{\partial y_t} \right]^T \in \Re^{2 \times 1},$$

$$\frac{\partial \boldsymbol{\tau}_k}{\partial (\cdot)} := \left[\frac{\partial \tau_{2k}}{\partial (\cdot)}, \frac{\partial \tau_{2k+1}}{\partial (\cdot)} \right] \in \Re^{1 \times 2}.$$

From here onward and for notational succinctness, we will drop the explicit dependency of matrices $\mathbf{G}_k$ on $(\sigma_{2k}, \sigma_{2k+1})$. The partial derivatives in (8) are obtained from (1) and (3). As an example the partial derivatives to compute $\mathbf{F}_1(\mathbf{x_t})$ are now given

$$\frac{\partial \tau_1}{\partial \mathbf{x_t^1}} = \frac{2}{c} \left[\frac{-(x_t - x_r)}{||\mathbf{x_t} - \mathbf{x_r}||}, \frac{(y_t - y_r)}{||\mathbf{x_t} - \mathbf{x_r}||} \right]^T$$
$$\frac{\partial \tau_2}{\partial \mathbf{x_t^1}} = \frac{2}{c} \left[\frac{(x_t + x_r)}{||\mathbf{x_r^1} - \mathbf{x_t}||}, \frac{-(y_r - y_t)}{||\mathbf{x_r^1} - \mathbf{x_t}||} \right]^T \tag{9}$$
$$\frac{\partial \tau_3}{\partial \mathbf{x_t^1}} = \frac{1}{2} \frac{\partial \tau_1}{\partial \mathbf{x_t^1}} + \frac{1}{2} \frac{\partial \tau_2}{\partial \mathbf{x_t^1}}.$$

Using (9), the following matrix can readily be constructed:

$$\frac{\partial \boldsymbol{\tau_1}}{\partial \mathbf{x_t^1}} = \begin{bmatrix} \frac{\partial \tau_2}{\partial x_t} & \frac{\partial \tau_2}{\partial y_t} \\ \frac{\partial \tau_3}{\partial x_t} & \frac{\partial \tau_3}{\partial y_t} \end{bmatrix}^T. \tag{10}$$

The FIM, $\mathbf{F}_1(\mathbf{x_t})$ can now be constructed using (9) and (10). From (8), we note that if any one of the multipath preservers in (4), (5), or (7) is zero, then those corresponding FIMs are rank deficient and hence singular at the corresponding target locations.

The complete FIM incorporating all the multipath time delays and the direct path is given by

$$\mathbf{F}(\mathbf{x_t}) = \left[\frac{1}{\sigma_1^2} \frac{\partial \tau_1}{\partial \mathbf{x_t^1}} \left(\frac{\partial \tau_1}{\partial \mathbf{x_t^1}} \right)^T + \sum_{k=1}^{3} \left(\mathbf{G}_k \odot \frac{\partial \boldsymbol{\tau}_k}{\partial \mathbf{x_t^1}} \right) \right.$$
$$\left. \times \left(\mathbf{G}_k \odot \frac{\partial \boldsymbol{\tau}_k}{\partial \mathbf{x_t^1}} \right)^T \right]. \tag{11}$$

From (11), it is seen that richer resolvable multipath mechanisms improve the CRBs by adding more statistical information to the FIM. The same conclusion can be made if we were to include higher-order multipath from multiple reflections as discussed in Section 3, provided of course they are detectable. From (11), notice that for $\mathbf{F}(\mathbf{x_t})$ to be full rank and hence nonsingular, at least one matrix must satisfy

$$\exists k: \quad \text{rank} \left(\left(\mathbf{G}_k \odot \frac{\partial \boldsymbol{\tau}_k}{\partial \mathbf{x_t^1}} \right) \left(\mathbf{G}_k \odot \frac{\partial \boldsymbol{\tau}_k}{\partial \mathbf{x_t^1}} \right)^T \right) \geq 1,$$
$$k = 1, 2, 3. \tag{12}$$

Equation (12) implies that apart from the direct path time delay, and regardless of the values assumed by the multipath preservers, at least one of the multipath time delays $\tau_p, p = 2, \ldots, 7$ must be detectable in the τ-domain. Indeed if it is known *a priori* that the target is shadowed (no direct path time delay, τ_1), then at least any two of the multipath time delays must be detectable or identifiable in the τ-domain.

Until now we considered only two dimensions, however, for the complete 3D problem, we may extend our results in a straightforward manner, for example, by taking the right-hand side of (12) to be 2 instead of 1, and with $\mathbf{x_t}$ now comprising the downrange, crossrange, and height parameters, and with suitable modification of the time delays to incorporate the 3D structure.

We now incorporate the multipath preservers formally into our FIM definitions. Define the regions, $\aleph$ and $\aleph_k, k = 1, 2, 3$ such that

$$\aleph := \{(-x, y) \mid 0 \leq x \leq D_1, D_y + y_r \leq y \leq D_2 + D_y + y_r\} \tag{13}$$

$$\aleph_k := \{(-x, y) \in \aleph \mid f_k(g_k(x, y)) = 1\}$$

where $\aleph_k \subseteq \aleph$, and $g_1(x, y) := y_A(\mathbf{x_r}, (x, y)), g_2(x, y) := x_B(\mathbf{x_r}, (x, y))$, and $g_3(x, y) := y_C(\mathbf{x_r}, (x, y))$. In other words, $\aleph$ consists of the entire region inside the urban canyon, and $\aleph_k$ are the regions inside the urban canyon where the

corresponding multipath preservers are unity. The FIMs can now be redefined as $\mathbf{F}_k := \mathbf{F}_k(\mathbf{x_t})\mathbb{1}[\mathbf{x_t} \in \aleph_k]$ and $\mathbf{F} := \mathbf{F}(\mathbf{x_t})\mathbb{1}[\mathbf{x_t} \in \bigcup_{k=1}^{3} \aleph_k]$. It is noted that one hand, $\mathbf{F}_k$ are evaluated at only those target locations which yield unit values for their corresponding multipath preservers. For all other locations $\mathbf{F}_k$ are rank-1 and hence singular, which implies that unbiased estimation of the target is not possible. On the other hand, it is clear that $\mathbf{F}$ is non-singular at those target locations where at least one of the multipath preservers are unity.

3.2 BCRBs

Assume that prior surveillance has made available the information that the target is located in a certain region inside the urban canyon in Figure 1b. As an example and an envisaged scenario, a prior unmanned aerial vehicle visit to the canyon has detected possible targets in a certain area, and has directed further investigation via a single-sensor, land-based radar. In such situations, BCRBs [16] are useful in analyzing the system performance.

Assume for simplicity that the target is uniformly distributed in $(-x_{\max}, y_{\max}) \times (-x_{\min}, y_{\min})$ inside the canyon. The joint probability density function of x_t and y_t is then,

$$p(x_t, y_t) = \mathbb{1}\left[(x_t, y_t) \in (x_{\max}, y_{\max}) \times (x_{\min}, y_{\min})\right] / (x_{\max} - x_{\min})(y_{\max} - y_{\min}).$$

Note that we may incorporate different distributions of the target priors; this uniform distribution example is just a simple initial example of how one would go about obtaining the BCRBs. Let us define the measured time delay vector, $\boldsymbol{\zeta} = [\zeta_1, \ldots, \zeta_7]^T$, and $p(\boldsymbol{\zeta}, x_t, y_t)$ as the joint pdf of $\boldsymbol{\zeta}, x_t$, and y_t. Then the BIM which considers multipath from all the walls is

$$\mathbf{B} = \mathbb{E}\left\{-\frac{\partial \ln p(\boldsymbol{\zeta}, x_t, y_t)}{\partial \mathbf{x_t^1}}\left(\frac{\partial \ln p(\boldsymbol{\zeta}, x_t, y_t)}{\partial \mathbf{x_t^1}}\right)^T\right\}$$

$$= \mathbb{E}\left\{\mathbb{E}\left\{-\frac{\partial \ln p(\boldsymbol{\zeta}|(x_t, y_t))}{\partial \mathbf{x_t^1}}\left(\frac{\partial \ln p(\boldsymbol{\zeta}|(x_t, y_t))}{\partial \mathbf{x_t^1}}\right)^T\right\}\right\}$$

$$+ \mathbb{E}\left\{-\frac{\partial \ln p(x_t, y_t)}{\partial \mathbf{x_t^1}}\left(\frac{\partial \ln p(x_t, y_t)}{\partial \mathbf{x_t^1}}\right)^T\right\}$$

$$= \mathbb{E}\left\{\mathbf{F}(x_t, y_t)\right\} + \mathbf{0} = \iint\limits_{x_t=x_{min}, y_t=y_{min}}^{x_{max}, y_{max}} \mathbf{F}(x_t, y_t)\, \mathrm{d}x_t\, \mathrm{d}y_t.$$

$$(14)$$

The zero matrix in (14) arises as the joint pdf $p(x_t, y_t)$ is a non-informative prior. For other distributions assumed, the second term will be non-zero. The BIM considering

the direct path and the multipath from the k-th wall is then given by

$$\mathbf{B}_k = \iint\limits_{x_t=x_{\min}, y_t=y_{\min}}^{x_{\max}, y_{\max}} \mathbf{F}_k(x_t, y_t)\, \mathrm{d}x_t\, \mathrm{d}y_t, \quad k = 1, 2, 3. \quad (15)$$

Like the classical CRBs, the BCRBs are present on the diagonals of the inverted BIMs. Unlike the FIMs, the BIMs are not a function of the target position vector, $\mathbf{x_t}$; they are a function of the radar location $\mathbf{x_r}$.

Some of the double integrals for computing the BIMs are intractable and expressed as integrals of elliptic integrals [17]. For example, consider the element in the first row, first column of matrix $\mathbf{B}_k, k = 1, 2, 3$. It is readily shown that the following term is required to obtain the BIMs:

$$I_a = \iint\limits_{x_t=x_{\min}, y_t=y_{\min}}^{x_{\max}, y_{\max}} \frac{x_r^2 - x_t^2}{||\mathbf{x_t} - \mathbf{x_r}||\,||\mathbf{x_r^1} - \mathbf{x_t}||}\, \mathrm{d}x_t\, \mathrm{d}y_t$$

Considering the integral w.r.t x_t, and decomposing the integrand into two parts, we have the following integrals I_b and I_c which are needed to obtain I_a:

$$I_b = \int\limits_{x_t=x_{\min}}^{x_{\max}} \frac{x_t^2}{||\mathbf{x_t} - \mathbf{x_r}||\,||\mathbf{x_r^1} - \mathbf{x_t}||}\, \mathrm{d}x_t,$$

$$I_c = \int\limits_{x_t=x_{\min}}^{x_{\max}} \frac{x_r^2}{||\mathbf{x_t} - \mathbf{x_r}||\,||\mathbf{x_r^1} - \mathbf{x_t}||}\, \mathrm{d}x_t$$

Now consider I_b, where $i := \sqrt{-1}$

$$I_b = \frac{-(I_1 - I_2)}{\gamma_1(x_r^2 + (y_t - y_r)^2)}, \quad I_1 := \int\limits_{x_t=x_{min}}^{x_{max}} \sqrt{\frac{1 - \gamma_1 x_t^2}{1 - \gamma_2 x_t^2}}\, \mathrm{d}x_t,$$

$$I_2 := \int\limits_{x_t=x_{min}}^{x_{max}} \frac{1}{\sqrt{1 - \gamma_1 x_t^2}\sqrt{1 - \gamma_2 x_t^2}}\, \mathrm{d}x_t,$$

$$\gamma_1 := \frac{-1}{((y_t - y_r) - ix_r)^2},$$

$$\gamma_2 = \frac{1}{(x_r - i(y_t - y_r))^2}. \quad (16)$$

We can write I_1 and I_2 as

$$I_1 = E(\sin^{-1}(\sqrt{\gamma_2}x_{\max}), \sqrt{\gamma_1/\gamma_2}) - E(\sin^{-1}(\sqrt{\gamma_2}x_{\min}), \sqrt{\gamma_1/\gamma_2}),$$

$$I_2 = F(\sin^{-1}(\sqrt{\gamma_2}x_{\max}), \sqrt{\gamma_1/\gamma_2}) - F(\sin^{-1}(\sqrt{\gamma_2}x_{\min}), \sqrt{\gamma_1/\gamma_2}),$$

where $F(\cdot, \cdot)$ and $E(\cdot, \cdot)$ denote the incomplete elliptic integral of the first and the second kinds, respectively, and

whose first and second parameters represent the complex amplitude and complex modulus, respectively [17]. Similarly the integral I_c may be evaluated employing the elliptic integral $F(\cdot, \cdot)$.

The above are an example of computations needed to evaluate one term in the BIM; there exist many such terms which are evaluated as integrals of $F(\cdot, \cdot)$ and $E(\cdot, \cdot)$. Numerical integration is employed in evaluating the BIMs for two reasons. First, the incomplete elliptic integrals are themselves evaluated numerically, see for example [17] and references therein. Second, it can be shown that the functions whose integrals we seek have no singularities in the region of interest as long as

$$\operatorname{supp} p(x_t, y_t) \subseteq \aleph, \quad \text{for any valid distribution } p(x_t, y_t),$$

where 'supp' denotes support. Numerical integration may produce erroneous results when regions include the singular points; but no such problems occur here since we consider only meaningful target priors, i.e., those whose supports are entirely inside the urban canyon.

4 Target or sensor positioning using statistical experimental design

The FIMs and BIMs not only provide us with theoretical bounds on localization error variance when exploiting resolvable multipath, but they may also be of use in designing radar experiments which seek to maximize the ability to exploit multipath. That is, radar operators may wish to either determine where targets are best localized, or where sensors must be placed in order to best localize (surveillance). These optimization problems may be posed in terms of statistical experimental design theory using several optimal design criteria [8].

4.1 Optimal positions for target localization given fixed radar position

Consider the situation where we have only a single wall, as in Figure 1a, with corresponding FIM $\mathbf{F}_1(\mathbf{x_t})$. The radar operator wants to know *a priori* where the target is best localized via multipath exploitation. Although in practice this is of course not in our control, but rather useful to know since estimated locations in the vicinity or at the optimal positions could be assigned as high confidence targets. Let us consider the *D*-optimal design, which maximizes the determinant of the FIM, and therefore minimizes the generalized variance of the optimal location estimate vector, $\hat{\mathbf{x}}_t$ [8]. Cast as an optimization problem for fixed $\mathbf{x_r}$, we have,

$$\max_{\mathbf{x_t}} \det \mathbf{F}_1(\mathbf{x_t}) \tag{17}$$

s.t $y_A(\mathbf{x_r}, \mathbf{x_t}) \leq D_2 + D_y + y_r, \quad -y_A(\mathbf{x_r}, \mathbf{x_t}) \leq -(D_y + y_r)$

Solving (17) via the Karush–Kuhn–Tucker (KKT) conditions, one can show there exist multiple optimal solutions for $\mathbf{x_t}$ which must satisfy

$$x_t^2 + (y_t - y_r)^2 - x_r^2 = 0, \quad \mathbf{A}_1 \mathbf{x_t} + \mathbf{b}_1 \leq \mathbf{0} \tag{18}$$

$$\mathbf{A}_1 := \begin{bmatrix} -(D_2 + D_y) & x_r \\ D_y & -x_r \end{bmatrix},$$

$$\mathbf{b}_1 := \begin{bmatrix} -x_r(D_2 + D_y + y_r) \\ x_r(D_y + y_r) \end{bmatrix}.$$

In (18) the first condition is an equation of a circle, whereas the second is the affine inequality constraint which is identical to the multipath preserver in (4) but in matrix form. Using the same approach, i.e. when we optimize $\mathbf{F}_k(\mathbf{x_t}), k = 2, 3$ instead, the corresponding circles are given by

$$\begin{aligned} \text{For } \mathbf{F}_2 : {}& (x_t + x_r)^2 + (y_t - D_2 - D_y - y_r)^2 \\ & - (D_2 + D_y)^2 = 0 \\ \text{For } \mathbf{F}_3 : {}& (x_t + D_1)^2 + (y_t - y_r)^2 - (D_1 - x_r)^2 = 0. \end{aligned} \tag{19}$$

The optimal target locations w.r.t. these walls must satisfy their corresponding circles in (19) and corresponding multipath preservers in (5), respectively. These optimal circles comprising the optimal target locations follow a simple pattern: *from the radar at $\mathbf{x_r}$ draw three lines, one to each wall, or its imaginary extension, which intersects it at a 90 degree angle. Then, the points of intersections with the walls or their extensions are the respective centers of the circles, and the distance of the centers from the radar location are the respective radii.* It is further stressed that these optimal circles in (18) and (19) are not to be confused with the iso-range contours or constant range loci traced by the target, as in (2).

The optimal target location w.r.t the full FIM (i.e., all walls together) is expressed as follows:

$$\max_{\mathbf{x_t}} \det \mathbf{F}(\mathbf{x_t}) \tag{20}$$

s.t $\quad y_A(\mathbf{x_r}, \mathbf{x_t}) \leq D_2 + D_y + y_r, \quad -y_A(\mathbf{x_r}, \mathbf{x_t}) \leq -(D_y + y_r)$

$\quad x_B(\mathbf{x_r}, \mathbf{x_t}) \leq D_1, \quad -x_B(\mathbf{x_r}, \mathbf{x_t}) \leq 0$

$\quad y_C(\mathbf{x_r}, \mathbf{x_t}) \leq D_2 + D_y + y_r, \quad -y_C(\mathbf{x_r}, \mathbf{x_t}) \leq -(D_y + y_r).$

The geometric insights resulting from the optimization problem are possible when we consider a *single* wall at a time, as in (17); however, we have not been able to obtain such analytically and intuitively succinct results when optimizing the full FIM (rather than the FIM for one wall at a time) as in (20). As such, the optimization is carried out numerically, and will be re-visited in the simulations in Section 6.

4.2 Optimal radar position for Bayesian target localization

Now consider positioning the sensor, when one has some form of *a priori* knowledge of the target location. This is well suited to a Bayesian approach where we seek to determine the sensor position $\mathbf{x_r}$ which minimizes the determinant of the BIM (again using D-optimal criteria). We start again by designing the best sensor position in the presence of one of the three walls at a time, i.e., we express this as three separate optimization problems:

$$\max_{\mathbf{x_r}} \det \mathbf{B}_k(\mathbf{x_r}), k = 1, 2, 3$$

$$\text{s.t} \quad \mathbf{x_r} \notin \aleph_p, \text{and } \mathbf{x_r} \in \Phi_k(\mathbf{x_t}) \tag{21}$$

where $\aleph_p := \text{supp } p(x_t, y_t)$ and

$$\Phi_1(\mathbf{x_t}) := \{\mathbf{x} | D_y + y_r \leq y_A(\mathbf{x}, \mathbf{x_t}) \leq D_2 + D_y + y_r, \mathbf{x_t} \in \aleph_p\}$$
$$\Phi_2(\mathbf{x_t}) := \{\mathbf{x} | 0 \leq x_B(\mathbf{x}, \mathbf{x_t}) \leq D_1, \mathbf{x_t} \in \aleph_p\}$$
$$\Phi_3(\mathbf{x_t}) := \{\mathbf{x} | D_y + y_r \leq y_C(\mathbf{x}, \mathbf{x_t}) \leq D_2 + D_y + y_r, \mathbf{x_t} \in \aleph_p\}.$$

The first constraint in (21) states that the radar position cannot be in the target prior pdf support. The second constraint states that a radar position is considered feasible if *all* target positions within the prior pdf's support satisfy their respective multipath preservers. It is not insightful to consider a particular radar position which does not satisfy the multipath preservers *for all* target positions within the support of the target prior pdf. It is noted that for the urban canyon this is NOT restrictive-since meaningful target priors are defined inside the urban canyon. Closed form solutions to (21) are intractable, but are evaluated numerically in Section 6.

The sensor positioning optimization for the general BIM (all walls together) is

$$\max_{\mathbf{x_r}} \quad \det \mathbf{B}(\mathbf{x_r})$$

$$\text{s.t} \quad \mathbf{x_r} \notin \aleph_p, \text{and} \mathbf{x_r} \in \bigcup_{k=1}^{3} \Phi_k(\mathbf{x_t}). \tag{22}$$

The first constraint in (22) is identical to that in (21). The second constraint states that a radar position is considered feasible if it belongs to least one of the $\Phi_k, k = 1, 2, 3$, as defined in (21). It is noted that there are several other design criteria, however as stated in ([8], p.153), D-optimal designs are practically relevant. A closed form solution to (22) is not possible, and the optimization will be performed numerically in Section 6. It is stressed that these computations may be performed offline, i.e., during the sensor deployment phase. In practice and unlike other optimization problems, it is noted here that the number of variables to be optimized is three or two, depending on the 3D or 2D model, hence computational complexity may not be an issue.

5 Other relevant topics pertinent to localization

It is stressed that the main focus of this article is to determine the performance bounds on single sensor target localization via multipath exploitation, as well as sensor and target positioning using statistical experimental design. In the previous sections, the experimental design techniques and the lower variance bounds on the target location were formulated under somewhat idealized assumptions: that the time-delays were already estimated and associated to each of the resolvable multipath components, that all reflections were specular, and that there was no clutter present. In this section however, we comment briefly on these ideal assumptions and their impact on target localization.

5.1 Multipath association

In (7), we assumed that we had estimates of the time-delays which were correctly associated with each of the multi-path returns (i.e., which wall and which path for that wall). Going back one step, in the measured range profile, even if the time delays are resolvable, they are not necessarily ordered as in $\tau_i, i = 2, \ldots, 7$. They are rather naturally ordered in an ascending order w.r.t their measured distances. The question is now, how to associate each of the time-delays to the different paths.

The first time delay, being the shortest, may be associated with the direct path. Labeling the remaining time delay peaks in the range profile may be accomplished by noting that the second order multipath, namely τ_p, $p = 2, 4, 6$ and the first-order multipath, namely τ_q, $q = 3, 5, 7$ share a linear relationship with the direct path, τ_1 given by,

$$\tau_q = \tau_1/2 + \tau_p/2. \tag{23}$$

Clustering first- and second-order multipath and wall association is briefly discussed next for completeness; more details are in [1]. Using (23) and employing a search using a least squares utility function, the first-order and second-order multipaths may be clustered together. Let us assume that the clusters are denoted as vectors given by $\boldsymbol{\tau}_A, \boldsymbol{\tau}_B, \boldsymbol{\tau}_C$. After clustering, their wall associations are still unknown. Since there are three clusters to be associated to the three walls, there exist 3! permutations. Let us denote the permutations or models as $\mathcal{M}_j, j = 1, 2, \ldots, 3!$. Let the mean vector under the assumption of correct wall association be denoted as $\boldsymbol{\tau}_o$. Now consider another model-dependent vector $\tilde{\boldsymbol{\tau}}(\mathcal{M}_j) = \mathbf{P}_j \boldsymbol{\tau}'$, where $\boldsymbol{\tau}' = [\tau_1, \boldsymbol{\tau}_A^T, \boldsymbol{\tau}_B^T, \boldsymbol{\tau}_C^T]^T$ and $\mathbf{P}_j$ are the associated permutation matrices, with the special case of $\mathbf{P}_1$ being the identity matrix of appropriate dimensions. With the distribution assumptions in (7), for the correct model, the random vector $\tilde{\boldsymbol{\tau}}(\mathcal{M}_j) - \boldsymbol{\tau}_o$ has zero mean, and for other incorrect wall associations, the mean is mis-specified and hence non-zero. Then, if we define $\mathbf{C}(\mathcal{M}_j)$ as the estimated

covariance matrix after say maximum likelihood estimation of the target location $\mathbf{x}_t$, then correct wall association given by the index $\hat{j}$ is deduced from

$$\hat{j} = \underset{j \in \{1,2,\ldots,3!\}}{\arg\min} \ \ln \det\{\mathbf{C}(\mathcal{M}_j)\} \qquad (24)$$

The location estimates at $\hat{j}$ are the estimates of the target locations at the correct wall association. The cost function in (24) is the standard information-theoretic model selection criteria, albeit without the penalizing function [18]. Not surprisingly, the penalty is irrelevant here since the free parameters for the 3! models are identical to one another. This implies that the error residuals (after maximum likelihood estimation) may be used equivalently instead of (24) for associating the multipath with the walls. Let us denote $\bar{\boldsymbol{\tau}}_o$ as the measured or extracted time delays whose elements are ordered identical to those in $\boldsymbol{\tau}_o$. Now if $\boldsymbol{\tau}_j(\hat{\mathbf{x}}_t^j)$ is the estimated time delay vector as a function of the jth location estimate $\hat{\mathbf{x}}_t^j$, then the jth model residual, $\mathcal{R}_j$, is defined as $\mathcal{R}_j = ||\bar{\boldsymbol{\tau}}_o - \boldsymbol{\tau}_j(\hat{\mathbf{x}}_t^j)||^2$.

5.2 Clutter

Clutter creates spurious time delay peaks in the radar range profile which are readily confused with genuine targets. However, clutter may be mitigated in certain circumstances. In urban scenarios where there is rich multipath, the assumption that targets are stationary may not necessarily be true, i.e., urban targets are often moving, albeit slowly. Furthermore, urban radar scenes consist of several stationary fixtures (or clutter), for example lamp-posts, billboards, signs, etc. which could highly be reflective. If a pulse-Doppler framework is advocated, then stationary clutter such as those described may be mitigated using simple moving target indication (MTI) techniques such as the delay line canceler [19]. For example, using the simplest two-tap delay line canceler results in the single sensor technique providing location updates repeatedly after two consecutive pulse repetition periods throughout the coherent processing interval (CPI). This is more than sufficient for urban targets since they are slowly moving.

In general, standard MTI may be sufficient to mitigate radar returns from stationary clutter, however, there could be scenarios where MTI is imperfect and clutter returns are persistent. Furthermore, MTI does not mitigate interactions between the moving targets and stationary clutter. For such relatively rare (but possible) scenarios, clutter manifests as spurious persistent peaks in the range profile. The multipath clustering search described in the previous section to label and cluster the first- and second-order multipath before wall association proves useful in isolating the clutter time delays, provided they are not confusable with the multipath returns, i.e., follow for example,

(23) with other multipath time delays. Simulation examples with extraneous clutter time delays, and application of the clustering to identify them is demonstrated in Section 6 for multiple targets.
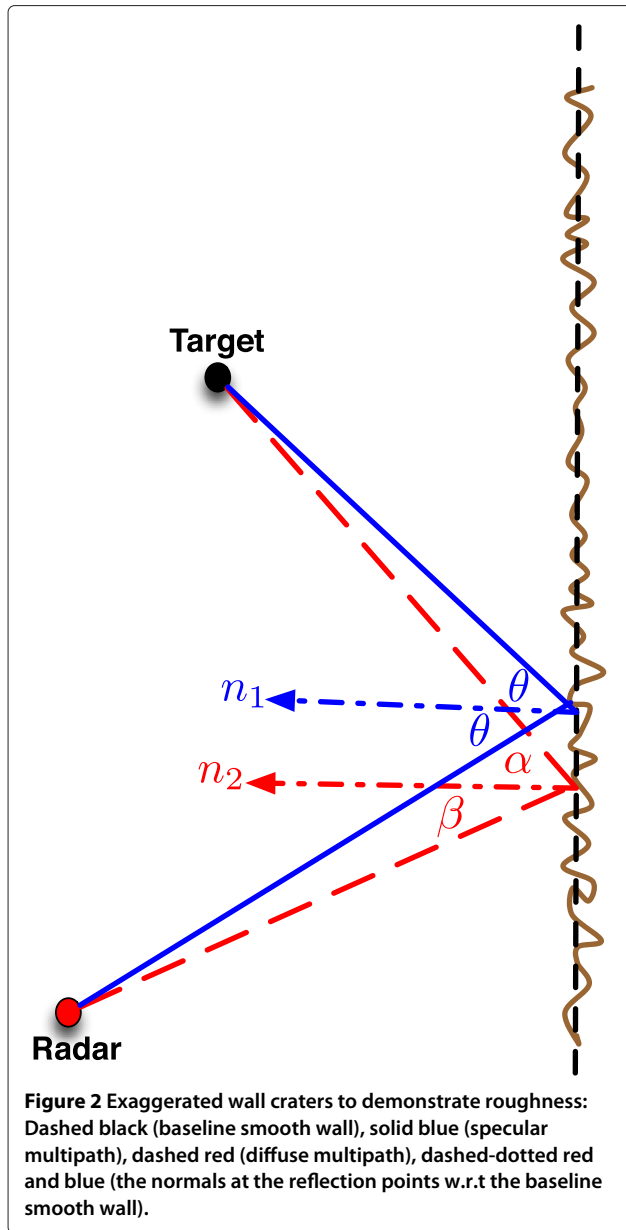
5.3 Impact of wall roughness

Thus far, we have considered smooth surfaces which result in ideal specular reflections for the multipath. We investigate if this is realistic, and whether wall roughness would impact localization via multipath exploitation. In particular, when the wavelength is comparable to the roughness/depth of groves (craters) in the walls, we ask whether this leads to severe scattering with several diffuse multipath components and smearing, and if so, how would it affect the time-delay estimates, when compared to the ideal case of smooth scattering from walls. To perfectly address the impact of wall roughness, a full investigation using electromagnetic (EM) theory would be needed; which necessitates, in part, knowledge of the material properties of the walls, and the various angles of incidence to compute the equivalent reflection coefficients but for the diffuse multipath components. Here, we take a higher-level signal processing approach and use simple, analytically tractable models to evaluate these effects, to obtain an approximate sense of the impact of wall roughness on localization.

EM conditions which describe wall roughness into classes, smooth, slightly rough, moderately rough, and very rough can be seen in [20], which furthermore provides a good introduction to modeling rough surfaces via radar. Interestingly, from [20], it maybe concluded that for a given incidence angle, a surface appears rough with decreasing wavelengths, and independent of wavelength, a surface appears smooth as the incident angle increases. Typically in urban scenarios, to facilitate operational covertness large standoff distances maybe employed, which lead to large incident angles for most walls. EM intensive bistatic and backscattering models for rough walls are beyond the scope of analysis here, but could be seen in [21-24] and references therein.

Consider Figure 2 which shows an exaggerated roughness texture of say wall-1. The solid blue line is the specular second-order multipath, and the red dashed-dotted line is one of the many diffuse second-order multipaths. The baseline smooth wall is also shown in this figure. The specular component has the angle of incidence w.r.t to normal n_1 equal to the angle of reflection, θ. Likewise in Figure 2, the diffuse component has the angle of incidence, α which is different and not equal to the angle of reflection β. It is noted that the normals are w.r.t the baseline smooth walls.

Our wall roughness model is based on using random perturbations to model roughness, as first pioneered by Rice [25], and used in for example [21-23] and references

Figure 2 Exaggerated wall craters to demonstrate roughness:
Dashed black (baseline smooth wall), solid blue (specular
multipath), dashed red (diffuse multipath), dashed-dotted red
and blue (the normals at the reflection points w.r.t the baseline
smooth wall).

therein. That is, to emulate roughness/craters on the wall,
we consider N subreflectors which form the length of the
wall(s). Each subreflector is placed at a random depth
from the baseline smooth wall. The random depths are
chosen from a Gaussian distribution with the means cor-
responding to the locations of the baseline smooth walls,
and the standard deviation as a percentage of the oper-
ating wavelength [5]. To simulate pattern roughness or
in other words texture, the random subreflectors may
be spatially correlated [5,25]. If the spatial correlation is
high, then the craters have a pattern to their roughness;
if not, then the roughness is un-patterned. The multipath
returns from the N subreflectors are superposed, with

each subreflector contributing diffuse multipath (the red
dotted lines in Figure 2).

Since the scattering properties of the random reflec-
tors are unknown, we will weight their contribution in
the radar returns. Selecting or modeling this weighting
function would be an excellent topic for an in-depth EM
investigation. Here however, we propose a simple but flex-
ible weighting model based on several physical realities in
the system. First, it may be shown (using constrained opti-
mization and Lagrange multipliers, for example) that the
length of the blue specular reflection multipath compo-
nent is smaller than any of the diffuse second-order (or
higher-order) red multipath components. This leads us to
design a weighting function as follows: if a subreflector is
closer to the specular point, the overall path length trav-
eled is shorter (and hence experiences lower path loss) and
its diffuse multipath component is weighted higher when
compared to the diffuse multipath from a subreflector
which is much farther away from the specular reflection
point on the wall. *It is however stressed that no specu-
lar multipath is intentionally incorporated into our model.*
This leads to "locally specular" return signal with many
diffuse components around the specular reflection but of
smaller magnitude.

The model will be evaluated via numerical simulations,
and the specific values assumed by the weighting and
spatial correlation are seen there. We note that both the
weighting and spatial correlation functions are selected
from a fairly general class of functions where one parame-
ter is tunable—this allows our model to incorporate a wide
variety of surfaces.

The diffuse multipath returns from rough walls may per-
turb the range-profile and hence the time-delay estimates,
which in turn will perturb the target location estimates.
We outline the relationship between the two next. Let
us consider a single wall at first. Assume that $\mathbf{\Delta x_t} :=
[\Delta x_t, \Delta y_t]^T$ is the resultant location perturbation arising
from perturbations in the time delays, $\Delta \tau_i$.

Consider the direct path, first- and second-order multi-
path from wall-1, then

$$\tau_1 + \Delta \tau_1 = \frac{2||\mathbf{x_t} - \mathbf{x_r} + \mathbf{\Delta x_t}||}{c},$$

$$\tau_2 + \Delta \tau_2 = \frac{2||\mathbf{x_r^1} - \mathbf{x_t} - \mathbf{\Delta x_t}||}{c},$$

$$\tau_3 + \Delta \tau_3 = \tau_1/2 + \tau_2/2 + \Delta \tau_1/2 + \Delta \tau_2/2. \qquad (25)$$

Subtracting (1) from (25), we obtain

$$\Delta \tau_1 = \frac{2}{c} \left[\frac{||\mathbf{x_t} - \mathbf{x_r} + \mathbf{\Delta x_t}||}{||\mathbf{x_t} - \mathbf{x_r}||} - 1 \right] \times ||\mathbf{x_t} - \mathbf{x_r}||$$

$$\Delta \tau_2 = \frac{2}{c} \left[\frac{||\mathbf{x_r^1} - \mathbf{x_t} - \mathbf{\Delta x_t}||}{||\mathbf{x_r^1} - \mathbf{x_t}||} - 1 \right] \times ||\mathbf{x_r^1} - \mathbf{x_t}||$$

$$\Delta \tau_3 = \Delta \tau_1/2 + \Delta \tau_2/2 \qquad (26)$$

Equation (26) maybe simplified further, in particular $\Delta\tau_1$ and $\Delta\tau_2$ maybe rewritten as

$$\Delta\tau_1 = \frac{2}{c}\left[\sqrt{1 + \frac{||\mathbf{\Delta x_t}||^2}{||\mathbf{x_t} - \mathbf{x_r}||^2} + \frac{2(\nabla||\mathbf{x_t} - \mathbf{x_r}||)^T}{||\mathbf{x_t} - \mathbf{x_r}||^2}\mathbf{\Delta x_t}} - 1\right]$$
$$\times ||\mathbf{x_t} - \mathbf{x_r}|| \qquad (27)$$

$$\Delta\tau_2 = \frac{2}{c}\left[\sqrt{1 + \frac{||\mathbf{\Delta x_t}||^2}{||\mathbf{x_r^1} - \mathbf{x_t}||^2} + \frac{2(\nabla||\mathbf{x_r^1} - \mathbf{x_t}||)^T}{||\mathbf{x_r^1} - \mathbf{x_t}||^2}\mathbf{\Delta x_t}} - 1\right]$$
$$\times ||\mathbf{x_r^1} - \mathbf{x_t}||$$

where $\nabla(\cdot)$ is the gradient operator with respect to $\mathbf{x_t}$. In (27), we ignore the (small) terms containing $||\mathbf{\Delta x_t}||^2$ in the square root. Using this and simplifying the resulting expressions with a binomial expansion results in a linear equation given by

$$\mathbf{\Delta\tau}_{w1} = \mathbf{A_1}\mathbf{\Delta x_t}$$

where $\mathbf{\Delta\tau}_{w1} := [\Delta\tau_1, \Delta\tau_2, \Delta\tau_3]^T$ and the matrix $\mathbf{A_1}$ is given by

$$\mathbf{A_1} = (2/c)\left[\nabla(||\mathbf{x_t} - \mathbf{x_r}||), \nabla(||\mathbf{x_r^1} - \mathbf{x_t}||),\right.$$
$$\left.\nabla(||\mathbf{x_t} - \mathbf{x_r}||)/2 + \nabla(||\mathbf{x_r^1} - \mathbf{x_t}||)/2\right]^T.$$

The analysis until now was for a single wall, i.e., wall-1. Incorporating the corresponding matrices and time delay perturbations for the other two walls, we may write

$$\mathbf{\Delta\tau} = \mathbf{A}\mathbf{\Delta x_t} \qquad (28)$$

where the vector $\mathbf{\Delta\tau}$ consists of the direct and multipath time delay perturbations form the rough walls-1,2,3. The matrix $\mathbf{A}$ is similar to matrix $\mathbf{A_1}$ but in addition consists of gradient vectors of the multipath time delays from the other two walls, and is straightforward to compute. The linear system in (28) is overdetermined with $\mathbf{\Delta x_t} = (\mathbf{A}^T\mathbf{A})^{-1}\mathbf{A}^T\mathbf{\Delta\tau}$ as the least squares solution. Equation (28) describes a deterministic relationship between the time delay and location perturbations. Since the wall roughness is modeled stochastically, the perturbation bias and perturbation variance of the location estimates can be analyzed via Monte Carlo simulations using (28), and are shown in Section 6.

We remark that when we incorporate wall roughness, location estimates are biased. It remains to be seen if target location estimates obtained from range profiles generated by EM models would also yield a bias. Nevertheless for biased estimates as such, the CRBs previously derived would not be immediately applicable, and biased CRBs could be derived instead [16]. However, if one were to obtain the target location biases *a priori*, then we would be able to offset their effect and use the derived CRBs directly. Formally incorporating wall roughness—via this stochastic model—into the previous CRBs and experimental design is not straightforward given that the wall

roughness model is random itself. When the wall roughness specifications are unknown, such as the location and the depth of each subreflector, which is true in practice, then, it may be more prudent to assume smooth walls and hence directly apply the results derived here.
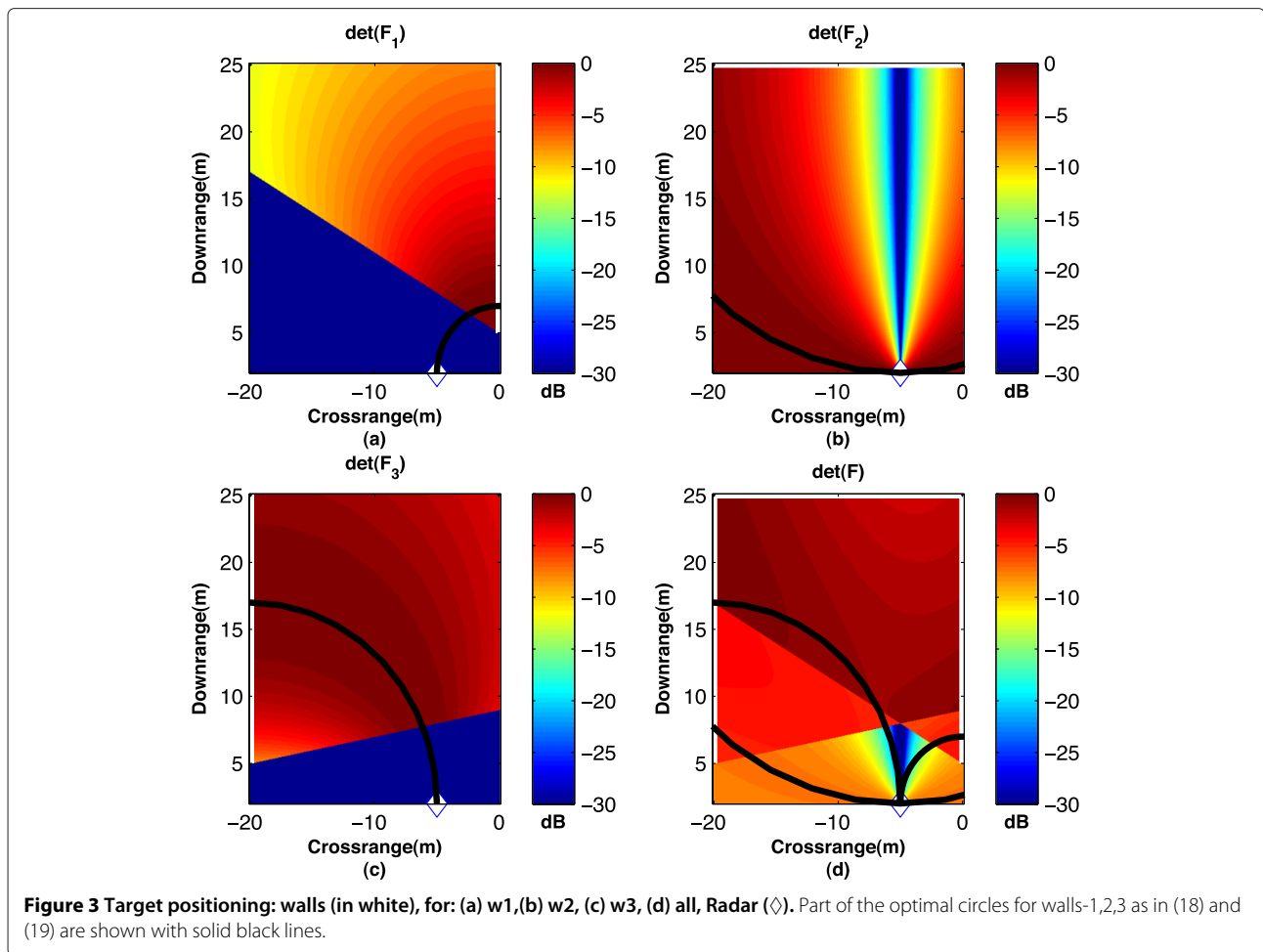
6 Simulations

We now proceed to examine various aspects of single-sensor localization through multipath exploitation using numerical simulations. All coordinates and dimensions are in meters unless specified otherwise. The standoff distance, $D_y = 3$, is assumed constant in all the simulations. The noise variance $\sigma_p^2 = \sigma^2, P = 1, 2...7$.

6.1 FIMs, multipath preservers, and target positioning

Figure 3 shows the determinant of the FIMs when the radar is assumed to be at position $\mathbf{x_r} = [-5, 2]^T$, shown as $\Diamond$. The target position is varied in downrange and crossrange inside the urban canyon whose dimensions are $D_1 = D_2 = 20$. In these figures, the determinant of the FIMs are first normalized (the value of σ^2 becomes irrelevant) by their maximum value and depicted in the dB scale. The dB scale is employed to clearly show the dynamic range of the experimental design criteria. Hereafter, the normalization as well as conversion to dBs will be employed for depicting the design criteria, unless mentioned otherwise.

In Figure 3a, we consider the direct path and the multipath from the first wall (w1) only, and det($\mathbf{F_1}$) is shown for varying downrange and crossrange target positions. The blue regions do not experience multipath (multipath blind), as predicted by its corresponding multipath preserver in (4). The multipath blind zones and visible regions w.r.t Figure 3a are shown in Figure 4a as a binary image. The determinants of the FIMs w.r.t the wall 2,3 are shown in Figure 3b,c, and the corresponding multipath blind and visible zones in Figure 4b,c. The corresponding walls are shown as solid white and red lines in Figure 3 and Figure 4, respectively. It is interesting to note that, for this geometry, multipath from the second, i.e., the back wall (w2) is always present, as the target's crossrange is varied within the canyon.

The determinant of the FIM when all the walls are considered is shown in Figure 3d. When considering walls 1, 2, or 3 individually, there exist several optimal target locations which maximize the determinant of their corresponding FIMs. As derived in (18) and (19), the optimal locations lie on circles which are also shown in Figure 3a–c therefore validating our analysis. The corresponding circles are also shown in Figure 3d. Interestingly, it is seen that the optimal locations lie above the intersection of these circles, and are closer to wall-3 and wall-1. A final important phenomenon is seen from Figure 3b: a deep notch all along the radar's crossrange position is observed.

Figure 3 Target positioning: walls (in white), for: (a) w1,(b) w2, (c) w3, (d) all, Radar ($\diamondsuit$). Part of the optimal circles for walls-1,2,3 as in (18) and (19) are shown with solid black lines.
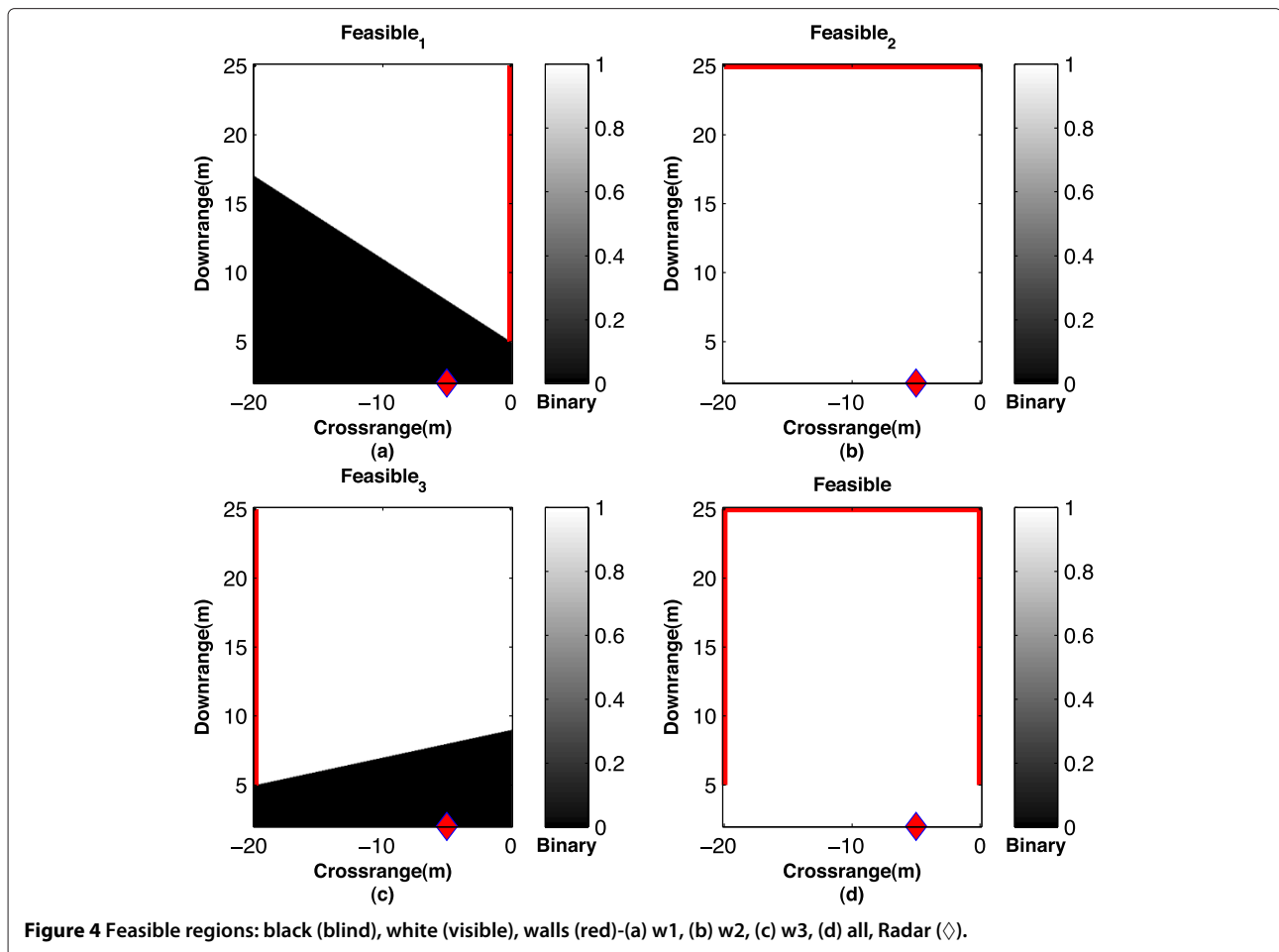
This is the shadow region, i.e., a region where, if a target was present, nothing behind it would be seen by the radar. Interestingly, the design criteria similar to (17) but for wall-2 chooses this as a multipath blind zone even though the multipath preserver formulation for wall-2 does not take into account whether a point of reflection is in the shadow region; the experimental design however does.

6.2 BIMs and sensor positioning

The application of sensor positioning via experimental design is demonstrated next. In Figure 5a–c, the determinant of the BIMs are shown when walls 1, 2, and 3 are considered independently, and in Figure 5d when they are considered together. As in the previous case, the multipath blind and visible zones can be inferred from Figure 6a–d, and are determined as explained in the paragraph following (21). In these figures, the target prior pdf is uniformly distributed over the square with $(x_{max}, x_{min}) = (6, 4)$ and $(y_{max}, y_{min}) = (16, 14)$, as shown by $\square$. The shadow region notches are now clearly seen in Figure 5a–c. If the sensor is placed at these notches, then those corresponding multipath delays will not exist and cannot be

used for subsequent exploitation. As mentioned before, these shadow region notches are placed automatically by the experimental design criteria and not by the multipath preservers. We see from Figure 5d that some of the optimal sensor positions are inside the canyon, and close to the target prior region. It is noteworthy that these optimal sensor positions are not on the boresight(s) of the target prior region. For covertness, it is clear from Figure 5d that the optimal sensor positions outside the canyon and away from the target prior will be preferred.

The sensor positioning w.r.t the FIMs are shown in Figure 7 for a target at the center of the prior region of the previous example. The results are more or less identical except that, due to the prior information, the values in the BIM scenario are slightly higher, but this cannot be seen due to the normalization employed. However, no straightforward comparisons can be made between the two since the former uses prior information, whereas the latter does not use the same. Identical shadow region notches are also clearly seen in the FIM scenario. The multipath blind and visible regions are shown only for walls 1 and 3 in Figure 8a,b, respectively.

Figure 4 Feasible regions: black (blind), white (visible), walls (red)-(a) w1, (b) w2, (c) w3, (d) all, Radar ($\Diamond$).

6.3 Multipath association, with and without clutter and higher-order multipath

We now provide a geometric interpretation of the multipath association algorithm for associating two targets in clutter and higher-order multipath. As detection is not the focus here, a simple peak picking strategy identical to the one used in [1] is used to extract the multipath time delays from the range profile. Three higher-order multipaths were considered for each of the two targets. The first higher-order multipath consists of the propagation from the radar to the target via one reflection each at walls-1,2, and returning by the same path. The second higher-order multipath consists of the one-way path propagation identical to the first higher-order multipath, but returning to the radar via one reflection at wall-2. Similarly, the third higher-order multipath consists of the one-way path similar to the first case, and the return path is via a single reflection at wall-3. The first higher-order multipath consists of four reflections in total, whereas the second and third consist of three reflections each.

To demonstrate the first- and second-order time delay clustering and wall association, a simulation example is

shown with white Gaussian noise added to the radar returns. We illustrate a form of "worst-case" analysis for clustering and associating multipaths with not one, but two targets in clutter which may arise from target–clutter interactions or from clutter remnants after MTI, and as described in Section 5. An SNR of 3 dB and two targets were assumed at locations $(-5.6, 11)$, and $(-16, 4.5)$. The noisy range profile after matched filtering is shown in Figure 9a. Extraneous time delay peaks representing the stationary clutter is shown in Figure 9a marked with two arrows. The true direct, true multipath, and true clutter time-delay peak locations are shown with $\Diamond$, and the true higher-order multipath locations are shown with $\triangleright$ in Figure 9a, respectively. For such-low SNR scenarios, we observed that over a small set of independent trials, several arbitrary noise peaks were selected, and the probability of correctly localizing both the targets was 60%. Theoretical detection criteria as well as rigorous Monte Carlo analysis are required to analyze the performance in low-SNR scenarios, and is not the main crux of this article. The true locations and the locations of the peaks after matched filtering are exact up to the second decimal place

Figure 5 Sensor positioning (BIM): walls (in white), For: (a) w1, (b) w2, (c) w3, (d) all, Target prior (□).
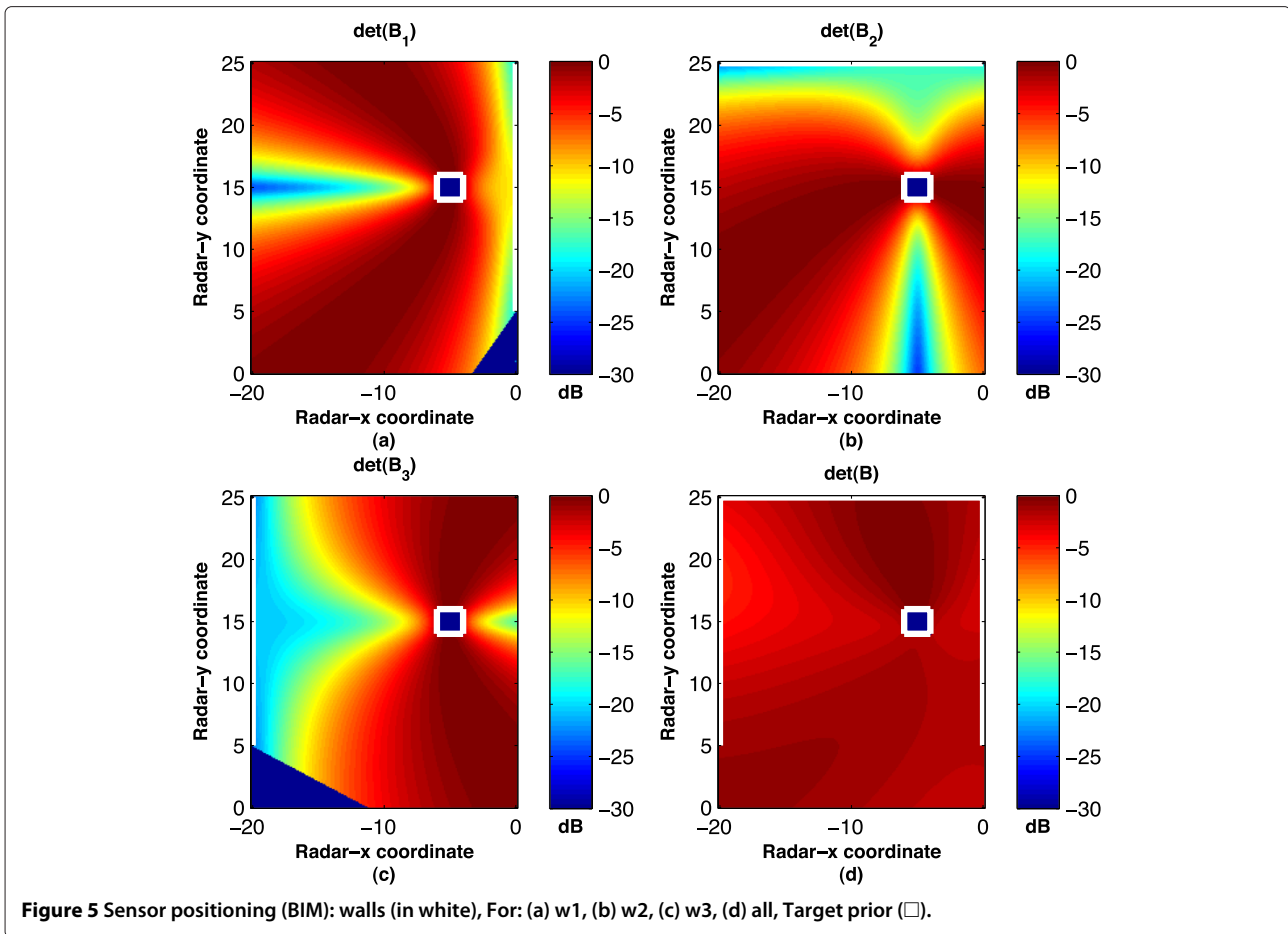
w.r.t the range. The true range of the direct and multipath peaks is given in Table 1. We outline first the clustering, and then the wall association algorithms and demonstrate their performance in simulations.

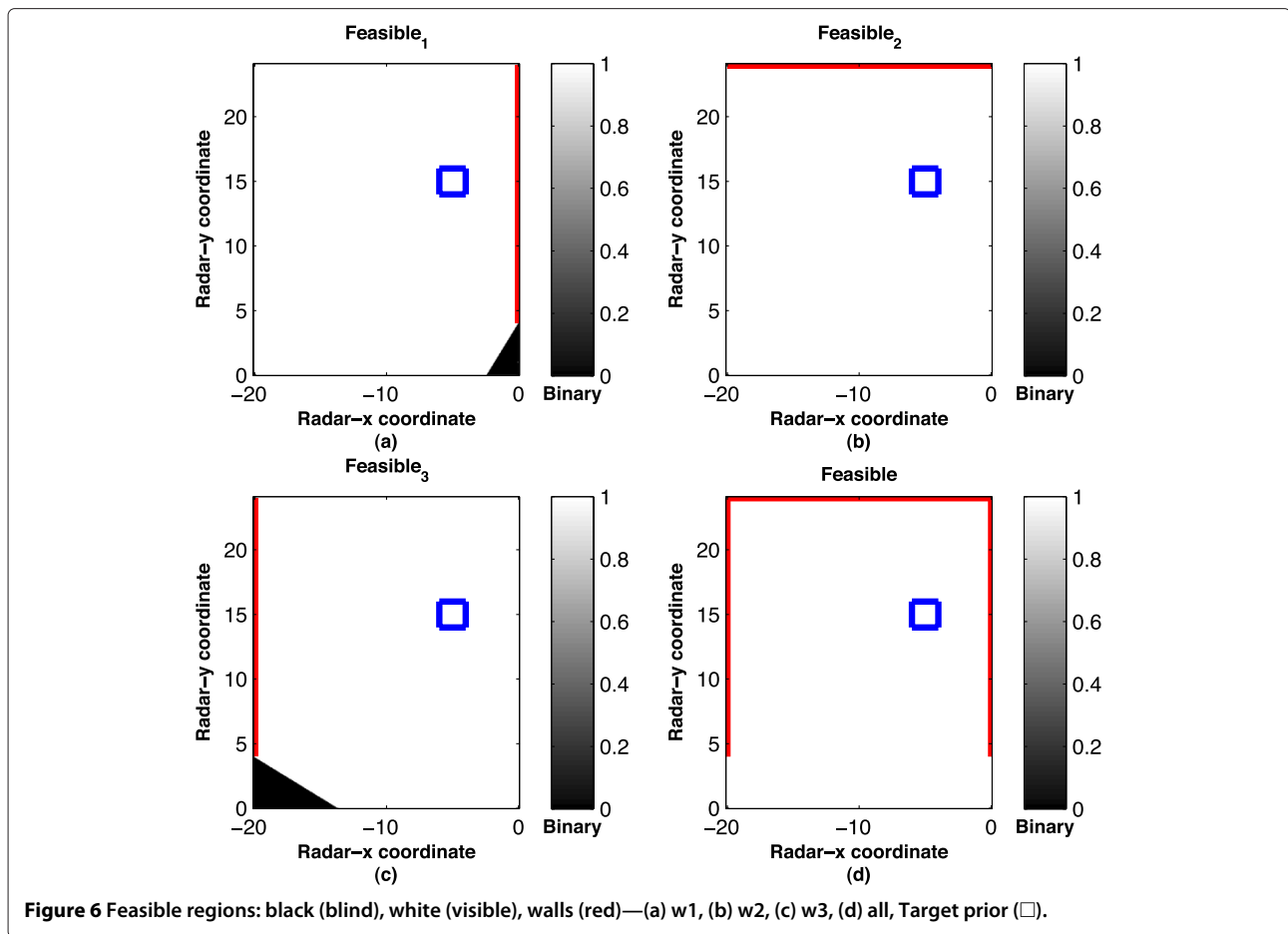### 6.3.1 Clustering of the first- and second-order multipath

From Table 1, and from Figure 9a, the first two peaks are at (6.02,9.41) in meters. The algorithm starts by assuming that the first peak is the direct path of some arbitrary target. The second peak is initially hypothesized as a first-order multipath, while the remaining peaks are candidate second-order multipaths. The relation between the direct path, I- and II-order multipath as in (23) is then used to identify the correct cluster. Applying this to the specific example, from the candidate II-order multipath time delay estimates, the peak at 12.81 m is selected. Hence (9.41, 12.81) are grouped. Using the same algorithm, the other peaks (15.91, 25.81) and (17.19, 28.35) are grouped for the direct path at 6.02 m. The second target's direct path, I, and II-order multipath are now clearly identified. Using the same principle, the first target's direct, I-, and II-order multipath are identified, whereas the clutter peaks at 15.33 and 22 m are outliers and are rejected

from the analysis. Similarly, the higher-order multipath are treated as outliers by the clustering algorithm and are rejected. After clustering or grouping the multipath, their wall associations are unknown and are dealt with next.

6.3.2 Wall association

There are six permutations for associating the grouped I- and II-order multipath pairs to the three walls. The permutation with the least cost (cost defined as in (24)), or equivalently corresponding to the least model fitting residual is then selected as the correct wall association.

The model residuals do not convey geometric insights to wall association, since they are merely numbers. However, the ellipses and circles as in (2), i.e., the iso-range contours do. The other ellipses and circles w.r.t walls-2,3 can readily be constructed. A straightforward relationship between the residuals and the circles and ellipses exist, and can readily be shown. For the correct wall association, the iso-range contours intersect at one location ideally, giving a low model residual. However, when the wall associations are incorrect, the iso-range contours do not all intersect at one location, resulting in a high model

Figure 6 Feasible regions: black (blind), white (visible), walls (red)—(a) w1, (b) w2, (c) w3, (d) all, Target prior (□).

residual. This thus allows us to visualize the wall association algorithm.

The ellipses and circles for the first and second target at the correct wall association is shown in Figure 9b. In this figure, the estimated target locations are shown as (blue square symbol). We have three ellipses corresponding to the I-order multipath from walls-1,2,3. Likewise for each target we have four circles, the circle centered at the radar (blue asterisk symbol) is the iso-range contours corresponding to the direct path. The other remaining circles are centered at the virtual radars (red asterisk symbol), and correspond to the iso-range contours of the II-order multipath from walls-1,2,3. Therefore, in total in Figure 9b we have 6-ellipses and 8-circles.

We examine the intersections of the elliptical and circular loci in Figure 10. In this figure, the circles and ellipses are shown for the six permutations. The grouped multipath corresponding to the first target located at $(-5.6, 11)$ was used. In Figure 10a, wall-1 association is correct whereas the rest are incorrect. In other words, the ellipses and circles corresponding to wall-1 correctly intersect at the right target location. Similarly, we see from Figure 10c,d that wall-2 and wall-3 associations

are correct, whereas the rest are not. In Figure 10f, all the ellipses and circles intersect the right target location; this is the correct wall association. It appears that Figure 10d,f is more or less identical. This is not true. The magnified version of Figure 10d in the inset shows three iso-range contours intersecting at one location, whereas the rest of the iso-contours intersect at different locations. In Figure 11a–f, similar elliptical and circular loci are shown but for the second target at $(-16, 4.6)$. The circles and ellipses in Figure 11f correspond to the correct wall association. Interestingly, due to ill-fitting some of the iso-range contours have purely complex parameters and are therefore not correctly rendered. For example, and are therefore not correctly rendered. For example, the ellipse corresponding to wall-2 association in Figure 11a,e has a complex minor-axis parameter, and is therefore not correctly shown.

The example assumed that clutter and higher order multipath was satisfactorily rejected by the clustering algorithm. In cases when the clutter or higher-order multipath time delays obey the relation (23) with some of the other single and double bounce multipath time delay peaks, they would be clustered incorrectly leading to erroneous
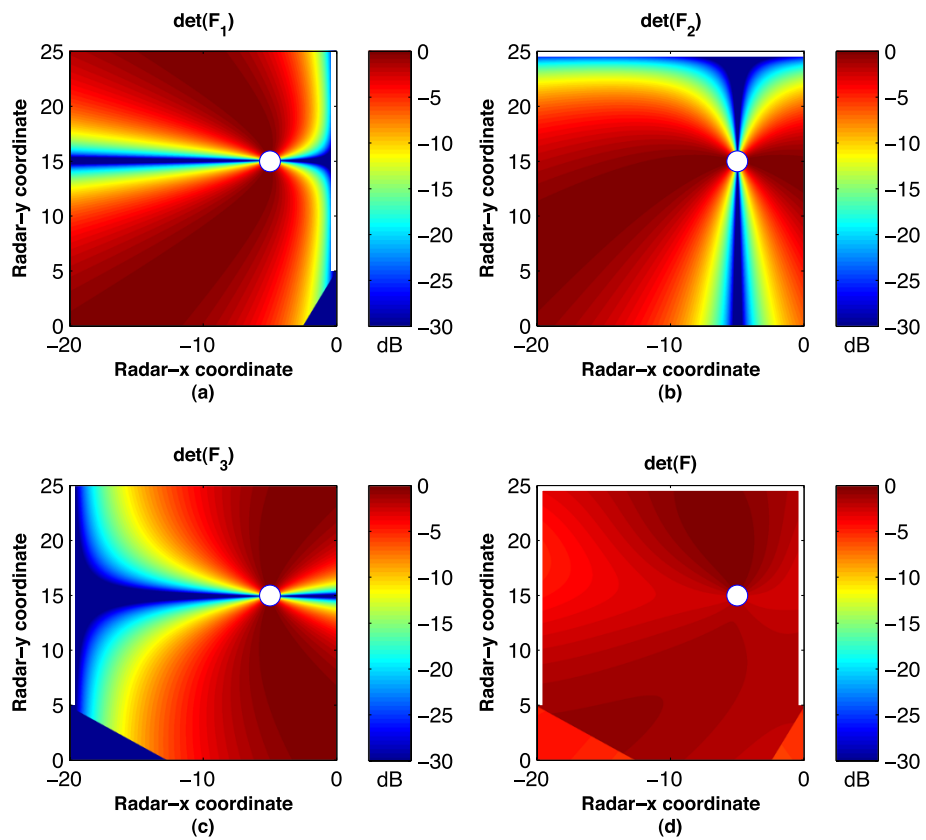
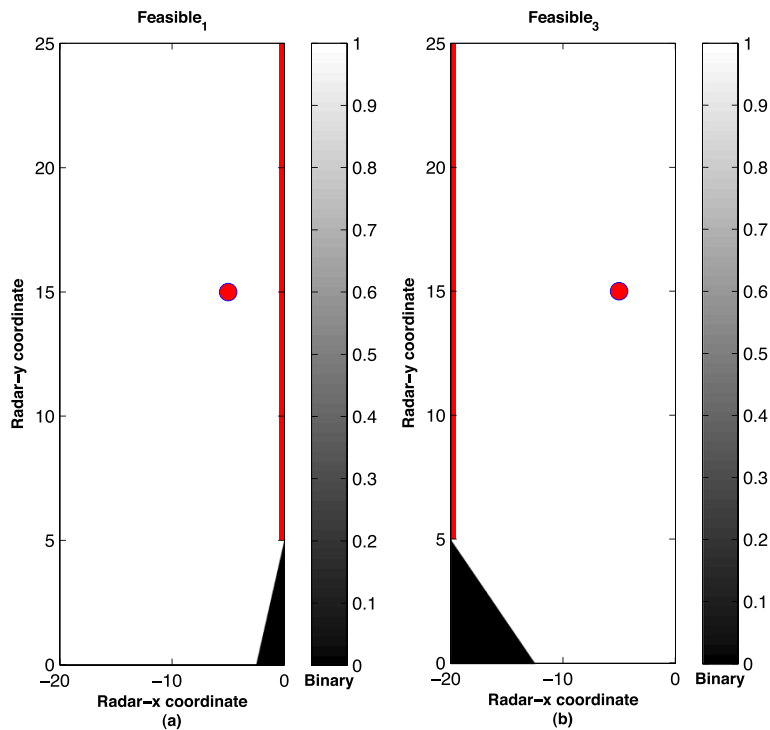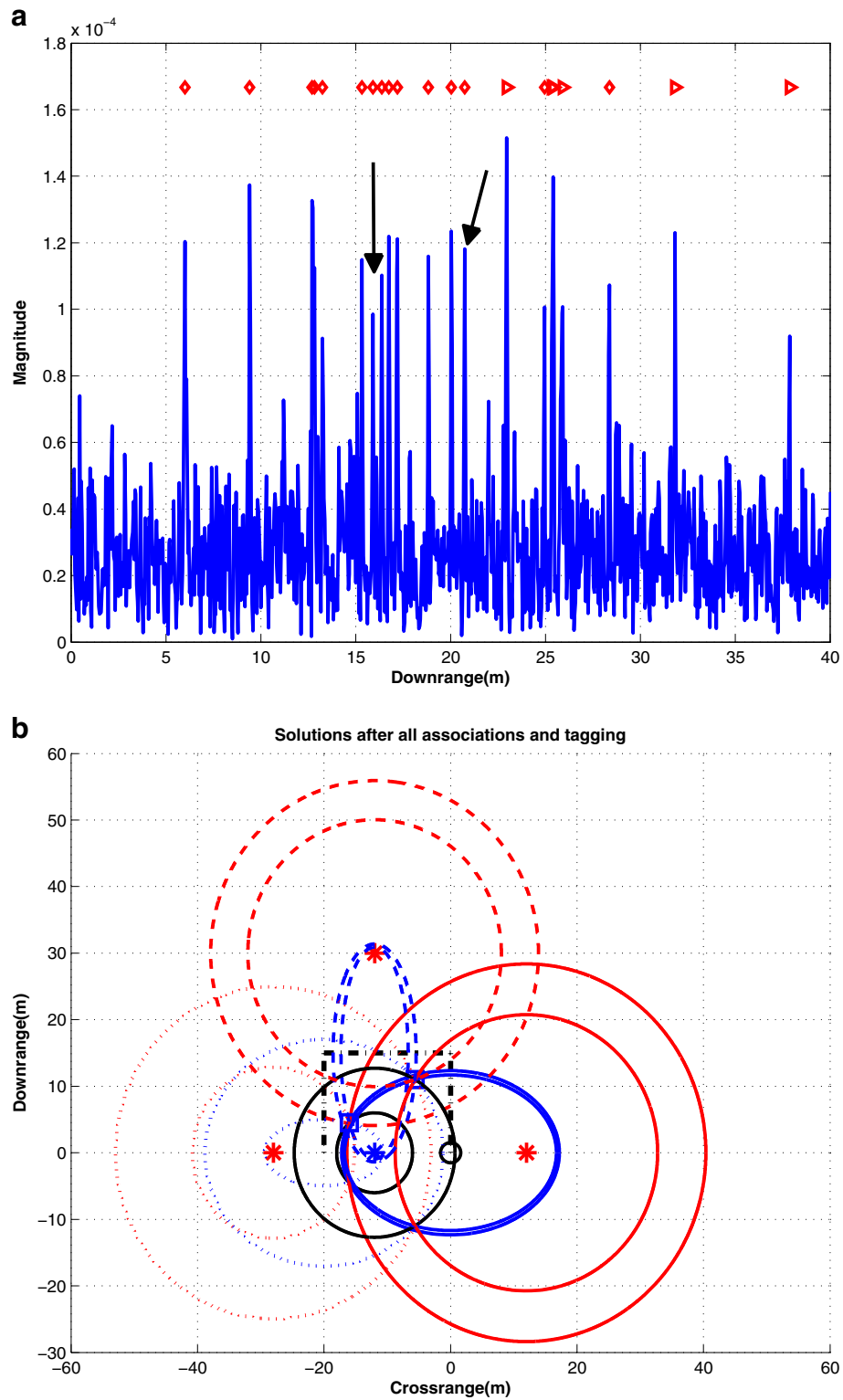**Figure 7 Sensor positioning (FIM): walls (in white), For: (a) w1, (b) w2, (c) w3, (d) all, Target (○).**

Figure 8 Sensor positioning feasible regions: - black (blind), white (visible), walls (red)—(a) w1, (b) w3, Target (○).

Figure 9 Two targets example. (a) 3-dB SNR range profile for two targets and with two clutter peaks (arrows) at 15.33 and 22 m, and few higher order multipath shown by (red triangle symbol), **(b)** elliptical and circular loci after clustering and wall association. In (b), direct path circles (solid black) centered at radar (blue asterisk symbol), bistatic ellipses (blue) and monostatic circles centered at virtual radars (red asterisk symbol), w.r.t wall-1 (solid), wall-2 (dashed), and wall-3 (dotted), and the intersections of the loci (blue square symbol) for the two estimated target locations.

Table 1 True range values of direct path (black), I-order multipath (blue) and II-order multipath (magenta) for first target at $(-5.6, 11)$ and second target at $(-16, 4.5)$

	Direct path	I-order multipath			II-order multipath		
		wall-1	wall-2	wall-3	wall-1	wall-2	wall-3
Target-1	12.72	16.74	16.38	18.84	20.75	20.04	24.95
Target-2	6.02	17.19	15.91	9.41	28.35	25.81	12.81

estimates. A combinatorial approach as in [1] could used but at a computational cost which increases exponentially with the number of targets or clutter time delay peaks. Nevertheless, due to the overdetermined system of equations, correct localization may be achievable by omitting the incorrect cluster from the analysis, provided it is identified easily from the circular and elliptical iso-range contour intersections.

6.4 Impact of wall roughness

Finally, we look at the impact of wall roughness on localization performance. Range profiles for rough walls after matched filtering are shown in Figure 12, for 1, 3, and 10% roughness in walls-1,2,3. The effects as seen in Figure 12 are for one random realization of the wall roughness percentages and for one instance of $N = 500$ equi-spaced randomly generated subreflectors for each wall. The locations of each subreflector on a particular wall is given by a 2D coordinate vector consisting of a deterministic x or y coordinate (depends on the wall), and the other coordinate (y or x resp.) whose location (depth) is randomly chosen. The carrier frequency was chosen to be 10 GHz in these simulations. The standard deviation of the random depths of the craters for each subreflector was chosen to be the roughness percentage w.r.t the operating wavelength. The statistical means of the random depths of the craters were assumed to be identical to the baseline smooth values, as if, the walls were smooth.

The spatial correlation of the random depths of the subreflectors are assumed to follow an exponential model with parameter η for walls-1,2,3. Similarly the weighting of the multipath returns from each subreflector are also assumed to follow an exponential model but with parameter γ. We denote $\mathcal{Z}_k$ as the *specular* deterministic x-coordinate (for $k = 2$) or the *specular* deterministic y-coordinate (for $k = 1, 3$) w.r.t wall-k, and similarly denote $\mathcal{P}_{kn}$ as the corresponding deterministic x-coordinate ($k = 2$) or the corresponding deterministic y-coordinate ($k = 1, 3$) of the nth subreflector, $n = 0, 1, \ldots, N - 1$. With similar notation let us denote $\mathcal{Q}_{kn}$ as the *random x-coordinate* ($k = 1, 3$) or *random y-coordinate* ($k = 2$). It is noted that $\mathcal{Z}_k$ and $\mathcal{P}_{kn}$ are deterministic, whereas $\mathcal{Q}_{kn}$ is random. The weighting function denoted as $\mathcal{W}(n, k)$ for the diffuse multipath radar return from the nth subreflector on the kth wall, and the spatial correlation function

denoted as $\mathcal{S}(n_1, n_2)$, between the n_1th and n_2th subreflector on the same wall, are given by

$$\mathcal{W}(n, k) = \exp(-\gamma|\mathcal{Z}_k - \mathcal{P}_{kn}|)$$
$$\mathcal{S}(n_1, n_2) = \exp(-\eta|n_1 - n_2|), \ (n_1, n_2) \in 0, 1, \ldots, N - 1$$

$$\mathcal{Z}_k = \begin{cases} y_A & k=1 \\ x_B & k=2, \\ y_C & k=3 \end{cases} \quad \mathcal{Q}_{kn} \sim \begin{cases} \mathcal{N}(0, \kappa^2\lambda_o^2) & k=1 \\ \mathcal{N}(D_2 + D_y + y_r, \kappa^2\lambda_o^2) & k=2 \\ \mathcal{N}(-D_1, \kappa^2\lambda_o^2) & k=3 \end{cases}$$

$$\mathcal{S}(n_1, n_2) = \left\{ (\mathcal{Q}_{kn_1} - \{\mathcal{Q}_{kn_1}\})(\mathcal{Q}_{kn_2} - \{\mathcal{Q}_{kn_2}\}) \right\},$$

where $\mathcal{N}(\cdot, \cdot)$ denotes the standard normal distribution, λ_o is the operating wavelength, and $\kappa = $ wall roughness %. The first- and second-order multipaths from each of these subreflectors are now weighted and superposed along with the direct path, and expressed as

$$s_{\text{rough}}(t) = s(t - \tau_1)$$
$$+ \sum_{k=1}^{3} \sum_{n=1}^{N} \mathcal{W}(n, k) \left(s(t - \tau_1/2 - \bar{\tau}_{kn}/2) + s(t - \bar{\tau}_{kn}) \right)$$

where $\bar{\tau}_{kn}$ is the second-order (double bounce) multipath time delay from the kth wall and nth subreflector, τ_1 is the direct path. The first-order multipath (single bounce) as before is sum of half the direct, and half the second-order multipath time delay. As a particular example, for $k = 1$, $\bar{\tau}_{1n} = 2||\mathbf{x_r} - \mathbf{u}_{1n}||^2/c + 2||\mathbf{u}_{1n} - \mathbf{x_t}||^2/c$, where the coordinate vector of the nth subreflector is $\mathbf{u}_{1n} = [\mathcal{Q}_{1n}, \mathcal{P}_{1n}]^T$ with $\mathcal{P}_{1n} \in [y_r + D_y, D_2 + D_y + y_r]$. Similar definitions are readily derived for $k = 2, 3$.

The parameters $\eta = 0.3$ and $\gamma = 0.3$ were used for generating Figure 12. The canyon dimensions are similar to those used in Figure 3, with the target located at $(-12, 22)$. The target RCS was unknown. Due to large number of diffuse multipath from walls-1,2,3, we made the target reflectivity slightly higher than the power from all the received diffuse multipath components. In practice, the strengths of the time delay peaks in the range profile will depend on several factors such as the monostatic RCS, bistatic RCS, and of course the material properties of the walls. If we order the peaks with descending order of magnitude, the second to the seventh largest peaks are the first- and second-order multipaths. Indeed we see other extraneous peaks which are attributed to wall roughness in Figure 12a–c, and in particular we also see that the extraneous peaks are stronger for the 10% wall roughness
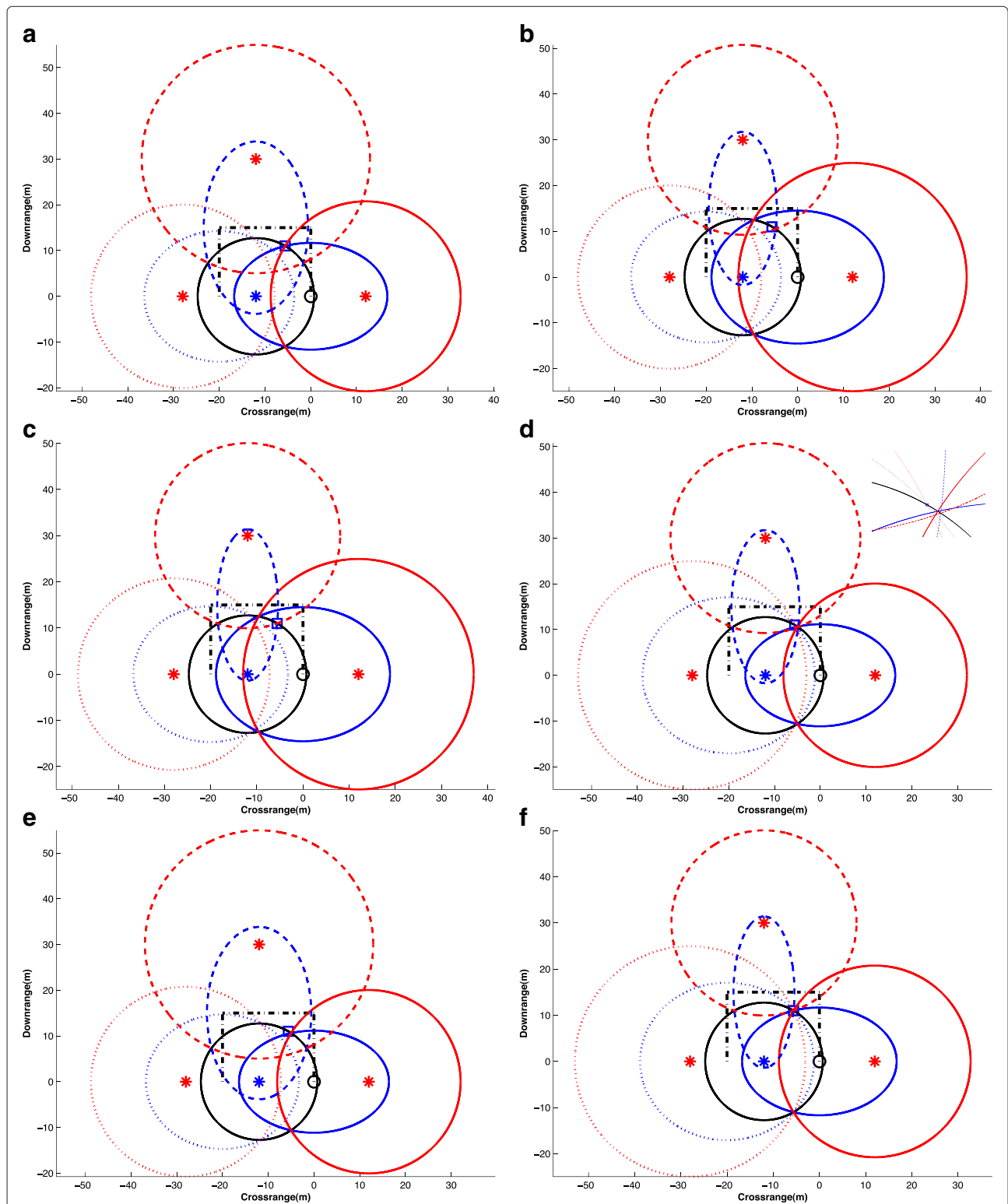
Figure 10 Non-coherent localization wall associations for the first target at $(-5.6, 11)$ **in Figure 9b, evaluated at the 3! permutations shown (a)–(f). (f)** Shows the correct association with the circles and ellipses intersecting at one common location. Plotting conventions are identical to Figure 9b.
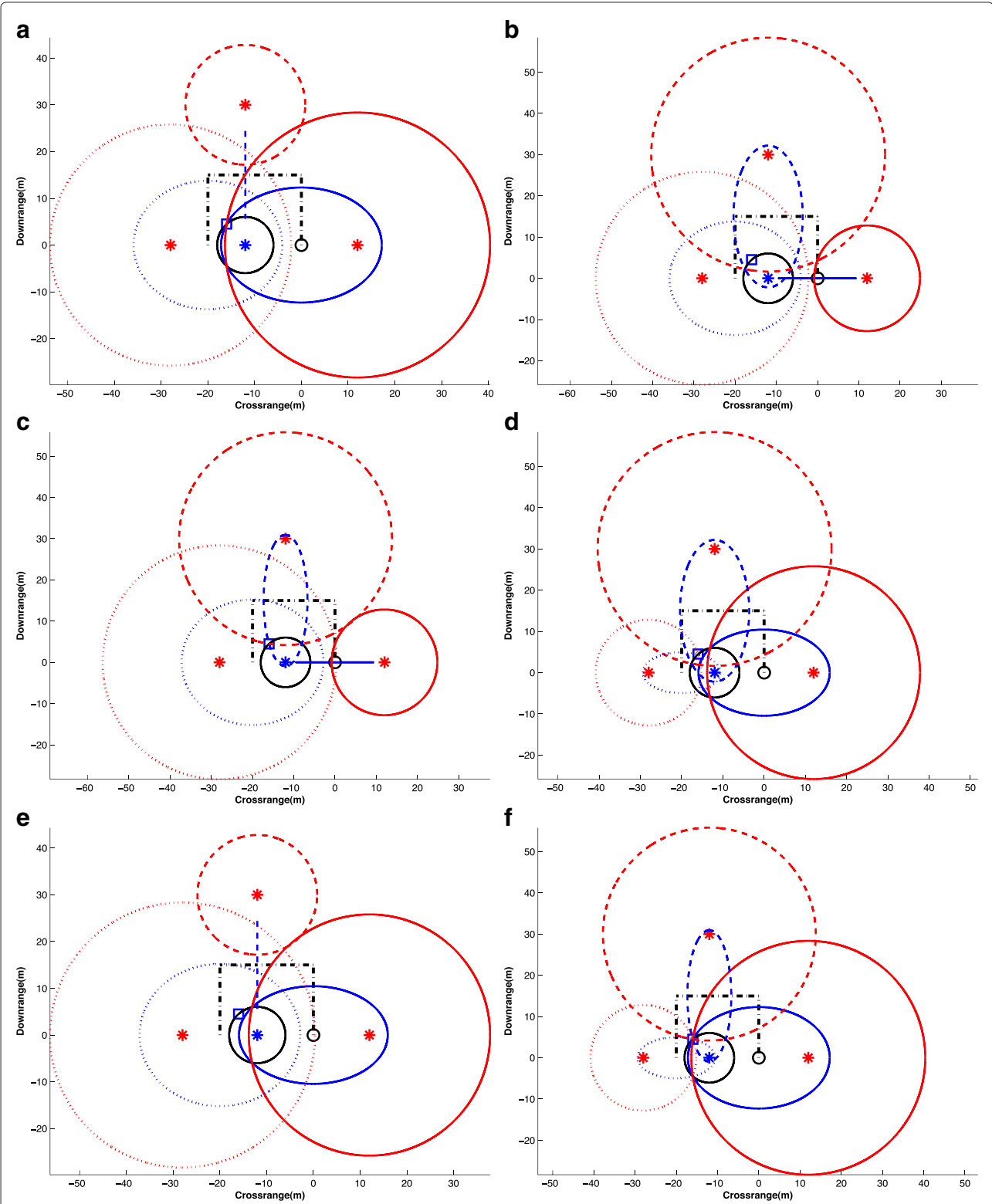
Figure 11 Non-coherent localization wall associations for the second target at $(-\mathbf{16}, \mathbf{4.6})$ **in Figure 9b, evaluated at the 3! permutations shown (a)–(f). (f)** Shows the correct association with the circles and ellipses intersecting at one common location. Plotting conventions are identical to Figure 9b.
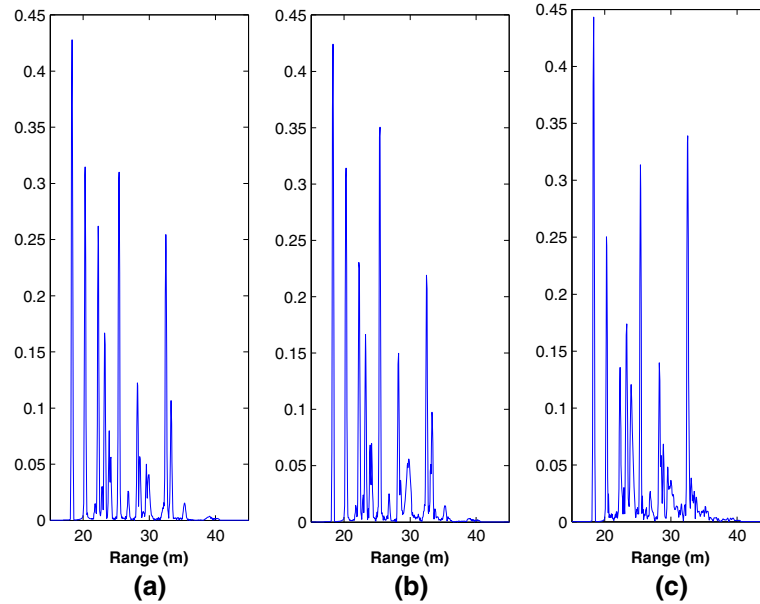
Figure 12 One realization of range profiles after matched filtering for (a) 1%, (b) 3%, and (c) 10% wall roughness.

case. The coherent loss of SNR is also seen in the first- and second-order multipath time delay peaks as they widely fluctuate in their magnitudes for different wall roughness percentages. In certain cases, we see that some of the peaks merge while some them split. All of these effects are due to the random constructive and random destructive phase effects due to the superposition of the diffuse multipath, and result in perturbation of the time delays leading to perturbation in locations of the target.

6.4.1 Impact of varying wall roughness and diffuse returns weighting.

To evaluate the mean perturbation and the variance of the target perturbation location error, 500 Monte Carlo trials were performed for varying wall roughness and varying γ.

The target location perturbation is derived from (28) for each trial. The mean and variance of the perturbation are given in Table 2. The locations of the local maximums in the range profile, within a 0.5-m search window on either side of the true locations of the time delays were used in the Monte Carlo analysis. In general from the table, and as expected, the localization perturbation bias increases, whereas the localization perturbation variance decreases for increasing wall roughness percentages. Likewise, both the perturbation bias and variance decrease with increasing weighting, i.e., γ. Surely, we see some examples especially for the 3 and 10% scenarios, when these trends are not followed. Not much attention needs to be focused on them, as they are attributed to the random effects and warrant more Monte Carlo trials which nevertheless are

Table 2 Perturbation statistics (downrange, crossrange) for fixed spatial correlation $\eta = 0.3$ and various wall roughness percentages and weighting parameter

Wall roughness (%)	1%	3%	10%
For $\gamma = 0.1$			
Perturbation bias (m)	(0.0246, 0.06)	(−0.0039, 0.0882)	(−0.0529, 0.1338)
Perturbation variance (m^2)	(0.0001, 0.0001)	(0.0022, 0.0011)	(0.0121, 0.0024)
For $\gamma = 0.3$			
Perturbation bias (m)	(0.0201, 0.0756)	(0.0037,0.0886)	(−0.0173, 0.1148)
Perturbation variance (m^2)	(0.0001, 0.0001)	(0.0008, 0.0008)	(0.0041, 0.0012)
For $\gamma = 0.6$			
Perturbation bias (m)	(0.017, 0.0787)	(0.0149,0.0802)	(−0.0057, 0.099)
Perturbation variance (m^2)	(0.000, 0.000)	(0.0002, 0.0002)	(0.0017, 0.0007)

Table 3 Perturbation statistics (downrange, crossrange) for 10% wall roughness percentage, for a fixed weight parameter $\gamma = 0.3$, and varying spatial correlation, η

Spatial correlation (η)	0.1	0.5	0.99
Perturbation bias (m)	$(-0.0207, 0.1097)$	$(-0.0212, 0.1189)$	$(-0.0210, 0.1237)$
Perturbation variance (m^2)	$(0.0023, 0.0012)$	$(0.0041, 0.0014)$	$(0.0044, 0.0014)$

computationally heavy. On a global scale such as the l_2-norm of the perturbation bias and variance, these trends are rather followed perfectly.

6.4.2 Impact of varying spatial correlation

The results for the 500 Monte Carlo trials for fixed roughness percentages, fixed weighting but for varying spatial correlation are shown in Table 3. An insignificant variation in the results are seen for varying values of η, implying that texture does not play a large role in target location perturbations. This is to be expected as the depth of subreflectors are on the order of wavelengths, which are in millimeters. Hence, their random correlated or random uncorrelated depths will not perturb the diffuse multipath time delays (range) significantly, therefore in general not affecting the perturbation statistics.

6.4.3 Impact of number of sub-reflectors

The results from the 500 Monte Carlo trials with varying number of subreflectors is shown in Table 4. The weighting, spatial correlation, and wall roughness are assumed fixed. As a trade-off between computations and accuracy, any value of N comparable to the operating wavelength as well as the wall dimensions maybe used for the wall roughness model. In our case, the wavelength corresponding to 10 GHz is 0.03 m. The maximum dimensions of the walls are 20 m in the $x - y$ dimensions. Hence, the dimension of each subreflector is 0.2 m for $N = 100$ and 0.01 m for $N = 2000$, both of which are comparable to the wavelength. Other values of N, for example $N = 10$, are not realistic in modeling rough walls for the considered wavelength. From this table when $N = 500$, the x-coordinate of the perturbation bias is higher, and may warrant more trials. However, the perturbation bias in the y-coordinate is more or less insensitive to changes in N. The perturbation variance shows insignificant variation w.r.t changes in N since the minimum value of N assumed already considers several diffuse resolvable and possibly several diffuse unresolvable multipath.

7 Conclusions and future directions

We have performed initial studies into the potential performance of the emerging area of single-sensor-based target localization scheme which exploits multipath returns, assuming they are resolvable and the geometry of the reflecting scene is known. To do so, we assumed a single target in a rectangular urban canyon comprised of three walls. For this geometry, Bayesian as well as the classical Cramér-Rao lower bounds on the target localization error variance were obtained. It was shown that each contributing multipath source, namely the walls, increases the FIM therefore improving the CRBs. Geometrical constraints, termed "multipath preservers" were derived to ensure that multipath was physically observable in the radar returns. Incorporating these into the D-optimal experimental design criteria, we demonstrated that FIMs and the BIMs aid in anticipating multipath blind zones, permitting optimal sensor or target positioning, and placing confidence levels on the multipath exploitation procedures. It was seen via simulations that the experimental design procedures discounted target or sensor positions in the shadow regions.

Wall roughness was incorporated into the radar returns, and its impact was shown on localization. Diffuse multipath from the craters on rough walls led to a bias in the location estimates when compared to the locations estimated from their smooth counterparts. As the wall roughness increases, the location bias increases. Wall association and multipath clustering were shown to be essential for correct localization, and were demonstrated using simulations, and their geometric interpretations, in the presence of extraneous clutter time delay peaks.

In the single-sensor paradigm, there is a scope for future research investigations along several directions. First, one may observe that when multipath is resolvable, it provides the radar operator with additional degrees of freedom. That is, from (7), we see that, in the urban canyon setting with three walls, there are seven multipath components (or equations) and two unknowns, i.e., the elements in

Table 4 Perturbation statistics (downrange, crossrange) for 10% wall roughness percentage, $\gamma = 0.5$, $\eta = 0.3$, but for varying number of subreflectors on walls-1,2,3

Number of subreflectors (N)	100	500	1000	2000
Perturbation bias (m)	$(-0.0072, 0.1152)$	$(-0.0109, 0.1052)$	$(-0.0017, 0.0980)$	$(-0.0067, 0.1040)$
Perturbation variance (m^2)	$(0.0032, 0.0008)$	$(0.0022, 0.0099)$	$(0.0019, 0.0005)$	$(0.0025, 0.0007)$

$\mathbf{x_t}$. Until now, we have assumed that the canyon dimensions namely, D_1 and D_2, are known, which is a standard assumption in the literature on multipath exploitation [1-7]. However, one may ask when it is possible to use the additional degrees of freedom to estimate the canyon dimensions, given that its geometry is rectangular? Surprisingly, it can be shown numerically that the FIM of the concatenated vector $[\mathbf{x_t}^T, D_1, D_2]^T$, denoted as $\mathbf{F}_{\text{all}}$, exists and is non-singular for those target locations satisfying $f_1(y_A) = f_2(x_B) = f_3(y_C) = 1$. Using radar returns including multipath to estimate building blueprints is not new and was part of the "visibuilding" program [26], possibly aimed at a multi-sensor sensing framework. However, since our approach uses a single sensor, a broad measurement campaign must be embarked upon to truly determine the potential of employing a single sensor in urban scenarios for estimating the canyon blueprint as well as the target location. Nevertheless at least analytically, when $f_1(y_A) = f_2(x_B) = f_3(y_C) = 1$, the non-singularity of the FIM $\mathbf{F}_{\text{all}}$ states that this is possible. Non-singularity of the FIM is a sufficient and necessary condition for (local) statistical identifiability [27]. Indeed in most cases, identifiable models implies estimable parameters [28], there are of course exceptions, see for example [29]. It is nevertheless hoped that the scenario as discussed with respect to the single sensor is not an example of such an exception.

Second, if a pulse Doppler framework is utilized, then the additional degrees of freedom provided by the Doppler could be used to improve multipath clustering performance, especially when confusable interactions between target and stationary clutter exists. When the Doppler information is fused, then the system will provide location updates for every CPI.

Finally, other future directions could include revisiting the perturbation bias and variance by using an EM intensive rough wall modeling, and compared with the results from the model assumed here. Sensitivity to localization should be examined when the canyon dimensions are slightly in error. Due to the over-determined nature of this problem, localization could still be possible when some of the multipath are not detectable or un-resolvable. Therefore, lastly and more importantly, algorithms to efficiently tackle such scenarios should be investigated.

Competing interests

Both authors declare that they have no competing interests.

References

1. P Setlur, GE Smith, F Ahmad, M Amin, Target localization with a single sensor via multipath exploitation. IEEE Trans. Aerospace Electron. Syst. **48**(3), 1996–2014 (2012)
2. S Sen, M Hurtado, A Nehorai, in *Proceedings of the International Waveform Diversity and Design Conference*. Adaptive OFDM radar for detecting a moving target in urban scenarios (Orlando, FL, February 2009), pp. 8–13
3. B Chakraborty, Y Li, JJ Zhang, T Trueblood, A Papandrous-Suppappola, D Morell, in *Proceedings of the IEEE International Conference on Acoustics, Speech, and Signal Processing*. Multipath exploitation with adaptive waveform design for tracking in urban terrain (Dallas, TX, March 2010), pp. 14–19
4. JL Krolik, J Farell, A Steinhardt, in *Proceedings of the IEEE Radar Conference*. Exploiting multipath propagation for GMTI in urban environments (Verona, NY, April 2006), pp. 24–27
5. R Linnehan, J Schindler, in *Proceedings of the IEEE International Radar Conference*. Multistatic scattering from moving targets in multipath environments (Pasadena, CA, May 2009), pp. 4–8
6. D Deiana, AS Kossen, WL van Rossum, in *Proceedings of the International Radar Conference*. Multipath exploitation in an urban environment using a MIMO surveillance radar (Vilnius, Lithuania, June 2010), pp. 16–18
7. KWK Liu, HC So, Range-based source localisation with pure reflector in presence of multipath propagation. Electron. Lett. **46**(13), 957–958 (2010)
8. A Atkinson, A Donev, R Tobias, *Optimum Experimental Design, with SAS*. (Oxford University Press, Oxford, UK, 2007)
9. AI Khuri, A note on D-optimal designs for partially nonlinear regression models. Technometrics. **26**(1), 59–61 (1984)
10. BM Sadler, RJ Kozick, in *Proceedings of the IEEE Workshop Sensor Array Multi-channel Signal Processing*. A survey of time delay estimation performance bounds (Waltham, MA, July 2006), pp. 282–288
11. T Dogaru, C Le, SAR images of rooms and buildings based on FDTD computer models. IEEE Trans. GeoSci. Remote Sens. **47**(5), 1388–1401 (2009)
12. P Setlur, M Amin, F Ahmad, Multipath model and exploitation in through-the-wall and urban radar sensing. IEEE Trans. GeoSci. Remote Sens. **49**(10), 4021–4034 (2011)
13. GE Smith, BG Mobasseri, in *Proceedings of the IEEE International Radar Conference*. Multipath exploitation for radar target classification (Atlanta, GA, May 2012), pp. 7–11
14. N Fourikis, *Advanced Array Systems, Applications and RF Technologies*. (Academic Press, New York, 2000)
15. P Setlur, Statistical algorithms and bounds for moving targets in urban sensing and through-the-wall radar applications, *PhD Thesis*, Villanova University (May 2010)
16. HL Van Trees, *Detection Estimation and Modulation Theory, Part I*. (Wiley-Interscience, New York, 2001)
17. *Digital Library of Mathematical Functions*, National Inst. of Standards and Tech. (2011). http://dlmf.nist.gov/
18. AD Lanterman, Schwarz, Wallace, Rissanen, intertwining themes in theories of model selection. Inter. Stat. Rev. **69**(2), 185–212 (2001)
19. MI Skolnik, *Introduction to Radar Systems*. (McGraw Hill, New York, 2001)
20. TG Farr, *Radar interactions with geologic surfaces*, (1993)
21. EI Thorsos, The validity of the Kirchhoff approximation for rough surface scattering using a Gaussian roughness spectrum. J. Acoust. Soc. Am. **83**(1), 78–92 (1988)
22. K Sarabandi, T Chiu, Electromagnetic scattering from slightly rough surfaces with inhomogeneous dielectric profiles. IEEE Trans. Antennas Propagat. **45**(9), 1419–1430 (1997)
23. A Tabatabaeenejad, M Moghaddam, Bistatic scattering from three-dimensional layered rough surfaces. IEEE Trans. GeoSci. Remote Sens. **44**(8), 2102–2114 (2006)
24. WS Ament, Forward and back-scattering from certain rough surfaces. IEEE Trans. Antennas Propagat. **4**(3), 369–373 (1956)
25. SO Rice, Reflection of electromagnetic waves from slightly rough surfaces. Commun. Pure Appl. Math. **4**(2–3), 351–378 (1951)
26. J Durek. http://www.darpa.mil/Our_Work/STO/Programs/Visibuilding.aspx, DARPA-STO, accessed July 2012
27. TJ Rothenburg, Identification in parametric models. Econometrica. **39**(3), 577–591 (1971)
28. J-M Dufour, C Hsiao, in *The New Palgrave Dictionary of Economics*. Identification (Palgrave MacMillan, Basingstoke, Hampshire, UK, p. 2008
29. A Gabrielsen, Consistency and identifiability. J. Econ. **8**, 261–263 (1978)